Technische Universität München
Ingenieurfakultät Bau Geo Umwelt
Lehrstuhl für Methodik der Fernerkundung
Univ.-Prof. Dr. Richard Bamler

Adaptation of an algorithm based on the two-dimensional Fast-Fourier-Transform (FFT) for the analysis of OH-airglow intensity measurements

Alexandra Kazlova

Master's Thesis

Master's Course in Earth Oriented Space

Supervisor(s):

1. PD Dr. –Ing. Adrian Doicu
German Aerospace Center (DLR)
Remote Sensing Technology Institute
Atmospheric Processors

2. Dr. Sabine Wüst
German Aerospace Center (DLR)
Remote Sensing Data Center
Atmosphere

October, 2015

Declaration

This thesis is a presentation of my original research work. Wherever contributions of others are involved, every effort is made to indicate this clearly, with due reference to the literature, and acknowledgement of collaborative research and discussions.

Munich,20.October.2015 ……

Abstract

Recent observational and theoretical studies of the properties of small-scaled gravity waves have highlighted the global effects on the circulation from the surface to the middle atmosphere. Airglow imaging allows to study small-scaled gravity waves in the mesopause (ca. ~87 km height). A new camera system is installed at DLR Oberpfaffenhofen with a narrow field of view and with the ability to take an image every 0.5 seconds which is quite new in the field of airglow imaging systems. The study is based on observations of 2014 year.

In this thesis an algorithm to analyze small-scaled gravity wave structures from the provided images of the airglow emission is described and adapted. The algorithm involves the two-dimensional Fourier analysis and can handle a large amount of data. It determines the horizontal wavelength and direction of propagation. The results are grouped monthly and compared to literature.

Contents

1. Introduction

In this work the adaptation of a 2D Fast Fourier Transform (FFT) algorithm for the analysis of OH-airglow images and first results are presented. The OH-airglow images were measured by infrared camera system at DLR Oberpfaffenhofen between January 2014 and December 2014. The camera system allows the observations of small-scaled atmospheric waves so-called gravity waves, with a temporal resolution of less than one second

An atmospheric wave is a periodic disturbance in time and space observable, in surface pressure or geopotential height, temperature or wind velocity etc. Atmospheric waves can be traveling or stationary wave, which means that they are propagate or stay stable over the same area. Gravity waves are an example for an atmospheric waves. They are generated between any stable layers of fluids of different density, when buoyancy forces try to restore the equilibrium, that transfer momentum from the troposphere to the stratosphere. Gravity waves are often created in the troposphere by frontal system or by airflow over mountains. They transport energy and momentum through the atmosphere and contribute therefore significantly to the coupling of the tropo-, strato- and mesosphere. Due to their impact on atmospheric circulation and structure, especially on mesosphere height, this waves are a subject of intense research activity in recent years. [Fritts and Alexander, 2003]

Modern studies of the global properties of small-scaled gravity waves highlighted the effect of these waves on the circulation from the surface to the middle atmosphere. However, the influence of small-scaled gravity waves have to be studied for both climate prediction and weather-forecast. Global-circulation models used for weather and climate prediction include unresolved gravity wave forcing via parametrizations. To reduce uncertainties in gravity waves parametrization a bigger amount of observation across the world should be done. Gravity waves are small in scale (less than 17km) and discontinuous in occurrence, therefore the measurements of gravity waves is a challenge. Recent technologies along with innovative analysis methods give more accurate information about the small-scaled waves. [Alexander et al., 2010]

Gravity waves can be observed through the observation of atmospheric airglow. Airglow self-lumenous layers which can be observed only during the night. It is due to chemical reaction of hydroxyl (OH, with emission altitude 87 km), molecular oxygen (O_2, 94 km) or atomic oxygen (O(I), 96 km). This study is focused on the OH-airglow emission. Gravity waves play an important role in modulation of these altitudes, temperature of the emission height and brightness of the emission itself. Observations from camera systems provide information about horizontal wavelength and periods of gravity waves. Most of the camera systems use a fish-eye lens for shooting entire night sky. Such a camera system normally produce one image per minute. [Leibniz-Institut für Atmosphärenphysik]

The camera system in this work has narrow field of view ($24^0 \times 19.5^0$), but with a comparatively high spatial resolution (output images of mesosphere have mean value of resolution 201 m^2). Currently it takes one image every 0.5 seconds, what is quite new in the

field of airglow imaging systems. Small-scaled gravity waves are the perfect object for the observation with such a camera system.

The work starts with a brief summary of physical fundamentals concerning atmospheric structure and waves as well as airglow. It is followed by information about the camera system and the image processing chain. In this work the focus is adaptation of a 2D-FFT algorithm for the extraction of horizontal wavelength and direction of propagation from OH-airglow images. Knowledge about wave parameters like wavelength, period and propagation direction is important in order to derive information about the amount of transported energy and the direction of energy transport. In chapter 3, a summary of the theory of the 2D FFT is provided first, afterwards the adapted 2D-FFT algorithm is described. The results split up according to month are shown in chapter 4 and discussed in chapter 5. The camera system is in operation since almost two years and a big amount of data is collected meanwhile. However not all of the data is appropriate for the future image processing. The main reason are mentioned, suggestions for improvements are given.

Also results from other research groups discussed and compared to the results of this work. Some ideas about the influence of mountains on gravity waves checked.

2. Atmosphere Physics

2.1. Atmospheric structure

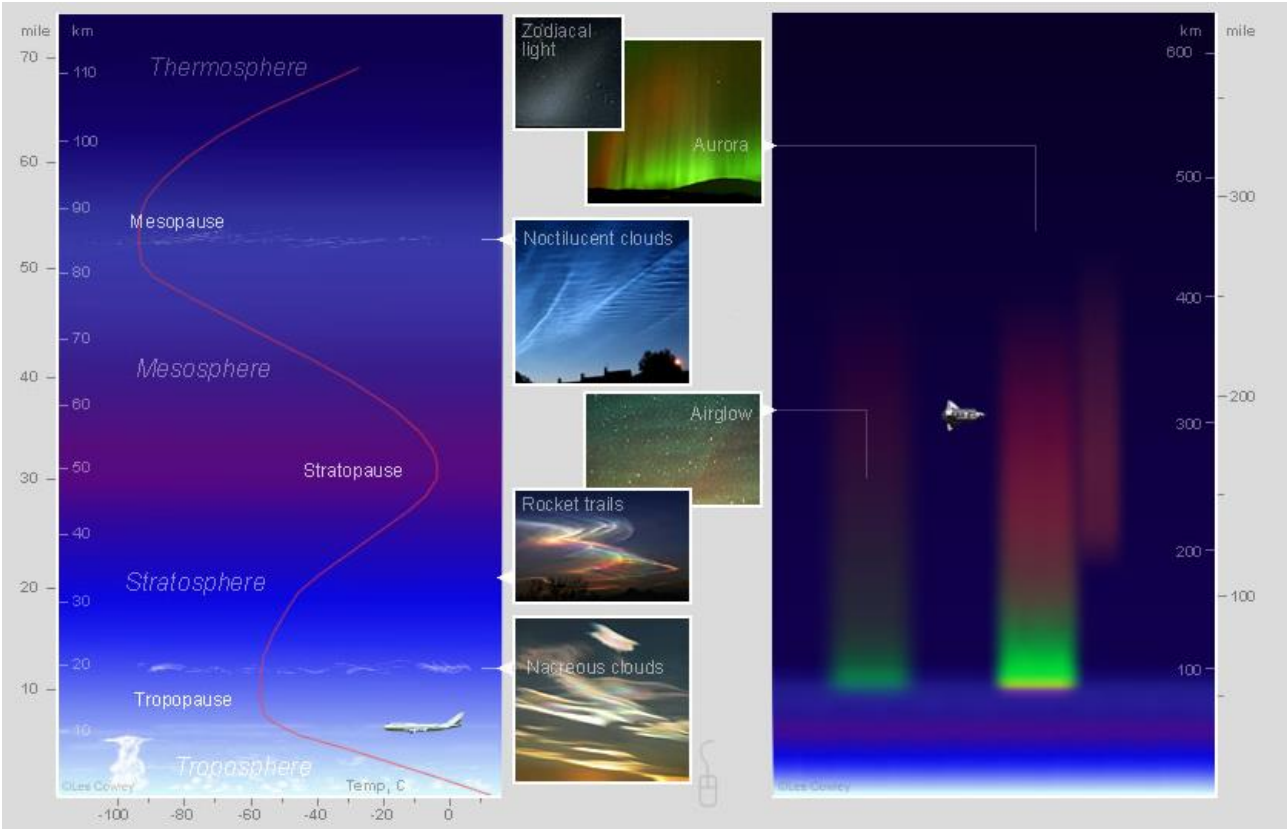

Figure 2.1 Earth's Atmosphere. *[http://www.atoptics.co.uk/hat1.htm]*

The Atmosphere is an important part of what makes Earth livable. The atmosphere composes of a mixture of ideal gases: although molecular nitrogen and molecular oxygen predominate by volume, the minor is constituents carbon dioxide, ozone and water vapour play important roles. The forcing of the atmosphere is primary from the Sun, though interactions with the land and the ocean are also important. The atmosphere blocks the high energy X-rays, most of Ultra-Violet and Infrared radiation from reaching Earth. It traps heat, making Earth a comfortable temperature. Many of the atmospheric processes can be described by thermodynamic principals, for example like cooling and heating of the atmospheric layers, according to its temperature gradient. The atmosphere is divided into five layers (see Figure 2.1). It is thickest near the surface and thins out with height.

- The TROPOSPHERE is the first layer above the surface and contains approximately 75% of the atmosphere's mass and 99% of its water vapor and aerosols. Weather occurs in this layer.

- The STRATOSPHERE is the second major layer of Earth's atmosphere. Here is located ozone layer where happens absorption of the sun radiation, mainly UV-radiation.
- Then goes MESOSPHERE layer, where meteors fragments usually burn up. OH-airglow layer is located here.
- The THERMOSPHERE is a layer with auroras. It is also where the space shuttle orbits.
- The atmosphere merges into space in the extremely thin EXOSPHERE. This is the upper limit of the atmosphere.

Figure 2.1 shows the atmospheric layer composition, the vertical structure of the temperature and one of the most significant events in each layer. The material for the chapter 2 is mostly taken from the [Andrews, 2005] and [Khomic et al., 2008]. The other sources and annotations are given directly in the text.

OH-airglow layer

Night sky on the Earth even with no interference from artificial lights, moonlight or aurorae, has a soft glow. This glowing is called airglow. Basically, it is a faint emission of light by a planetary atmosphere. The airglow is visible over the whole globe. The brightest part is 10-15 degrees above the horizon. For person unaided eyes it is not visible because its light is below the threshold of colour perception. From orbit it looks like a "green bubble" enclosing the planet. The brightest emission is green (558nm) from oxygen atoms in a layer 90-100 km height. The Figure 2.2 shows an image of the full sky taken by a fisheye lens camera. Green bands, stretch from east to west over the whole sky, are the gravity waves which are visible in the airglow layer.

The upper atmosphere of the Earth (above 80 km) consists with mostly atomic and molecular nitrogen and oxygen, along with hydrogen and helium. The small components, such as nitric oxide NO, carbon oxide CO, carbon dioxide NO_2, metastable atoms and molecules, are important for the photochemistry, energetics and emission of the upper atmosphere. The ionizing solar ultraviolet radiation gives rise to numerous photochemical processes in the atmosphere which induces the airglow. This glow happens both during the day and night time. It is possible to say that the airglow is the light of electronically and/or vibration-rotationally excited atoms and molecules at the attitude 80 km or higher. There are two strong airglow emission that are used mostly in studies of gravity waves: the OI green line emission and the OH near-infrared (or Meinel in some literature) band system emission. Main study of this work is OH-airglow.

The OH airglow comes from the production of rotational-vibrational excited OH (v) molecules, which emit photons during transitions to lower vibrational states. The chemical reactions leading to the production of OH (v) are given by next formulas:

$$H + O_3 \rightarrow OH(v) + O_2 \qquad Eq.\ 2.1$$

$$O + HO_2 \rightarrow OH(v) + O_2 \qquad Eq.\ 2.2$$

Reaction Eq. 2.1 is generally considered to be the main reaction to OH(v) production, from which lower vibrational states are excited by downwards cascade. Eq. 2.2 also contributes to the lower vibrational states OH(v). [Snively et al., 2010]

Figure 2.2 An all sky image by Doug Zubenel after local midnight in Cherry Country, Nebraska, august 2005. *[http://www.atoptics.co.uk/highsky/airglow1.htm]*

The central mechanism for formation of OH-airglow is the Bates-Nicolet reaction between ozone and hydrogen atoms, as was mentioned before, which is described by Bates and Nicolet in 1950. The OH airglow is limited at higher altitudes by the rapid fall off in ozone concentration with height and at lower levels by the onset of the rapid quenching of the excited products by collision more frequent at the higher atmospheric pressure. The balance between the two limiting processes creates the narrow OH airglow layer. Intensity of the OH emission layer peaks locates near 87 km altitude, with 8 km full width at half maximum. The relative volume emission rate based on the satellite instrument TIMED SABER over Oberpfaffenhofen area is plotted on the Figure 2.3.

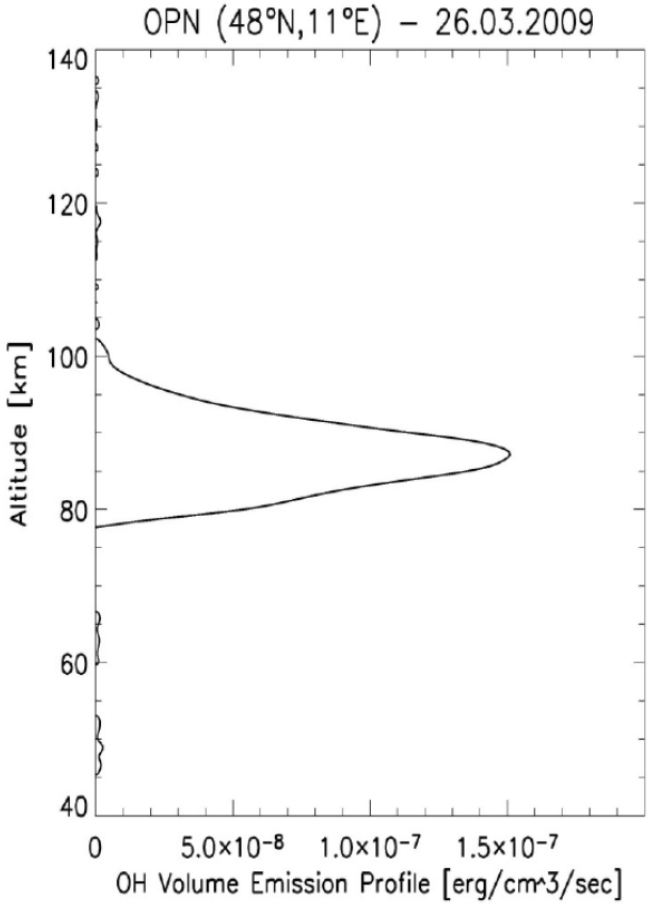

Figure 2.3 OH volume emission profile over Oberpfaffenhofen (26.03.2009).

Van Rhijn effect

Measurements of the airglow layer show that intensity increases systematically from the zenith to the horizon. It is known that the layer responsible for the emission has a constant height and uniform thickness and brightness, than the increase in intensity toward the horizon means that it represents a function of height, this effect was first shown by van Rhijn in 1924. There is also the lack of uniformity of the emission layer over the sky, but since the camera, used for this study, has a narrow angle, that is why uniform thickness and brightness are assumed. The geometry of the camera's collimation axis propagation over Atmosphere is shown on the Figure 2.4. This also helps to understand why preprocessed image get a shape of trapezium.

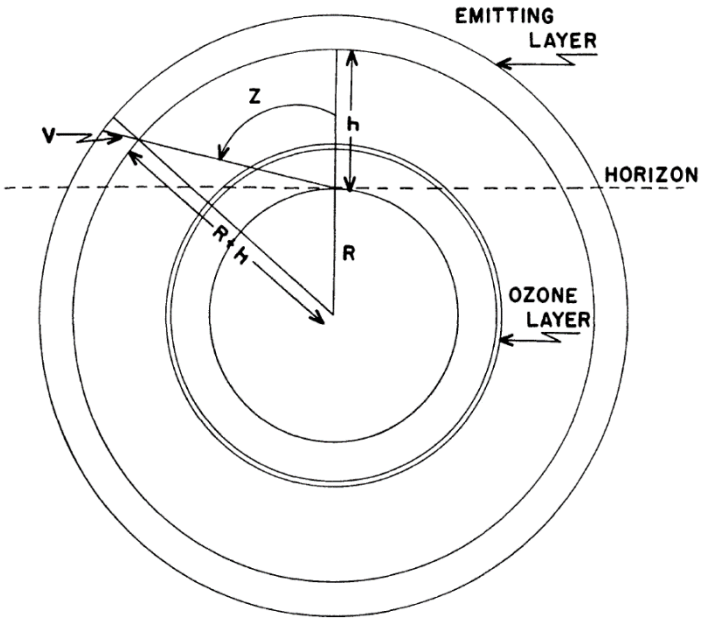

Figure 2.4 Schematic sketch of layers in the earth's upper atmosphere. [Roach et al.,1955]

The main function for the calculation of the path length through the upper layer is given by.

$$V=\frac{1}{\sqrt{\{1-[R/(R+h)]^2 sin^2 z\}}} \qquad \textit{Eq. 2.3}$$

where *z* is zenith distance, *R* is radius of the Earth, *h* is the height of the emitting layer above the observer, *V* is a relative path length. [Roach et al., 1955]

2.2. Gravity waves

Atmospheric waves can be distinguished according to their restoring force. Among planetary and sound waves, there exist gravity waves. Gravity waves are generated between any stable layers of fluids of different density. The smooth vertical density variation in the atmosphere is approximated by a stack of thin fluid layers, whose densities decrease with height. When the fluid boundary is disturbed, buoyancy forces try to restore the equilibrium. Sometimes, they are called buoyancy waves, since their existence depends on the buoyancy. The fluid returns to its original shape, overshoots and oscillations then set in which propagate as waves. Atmospheric gravity waves are analogous to horizontally propagating waves on water, which depend on the restoring mechanism provided by the contrast in density between air and water.

Gravity waves are generated in many ways, like air flow over mountains (see Figure 2.5) and convective activity in the troposphere. Propagation of the waves from the lower atmosphere upwards into the stratosphere and mesosphere is possible under certain circumstances. Due to decreasing of air density with height, the amplitudes of the wave

fluctuations will grow as long as the wave's energy is conserved. Hence, gravity waves can attain large amplitudes in the mesosphere and exert a considerable influence on the mean atmospheric state there.

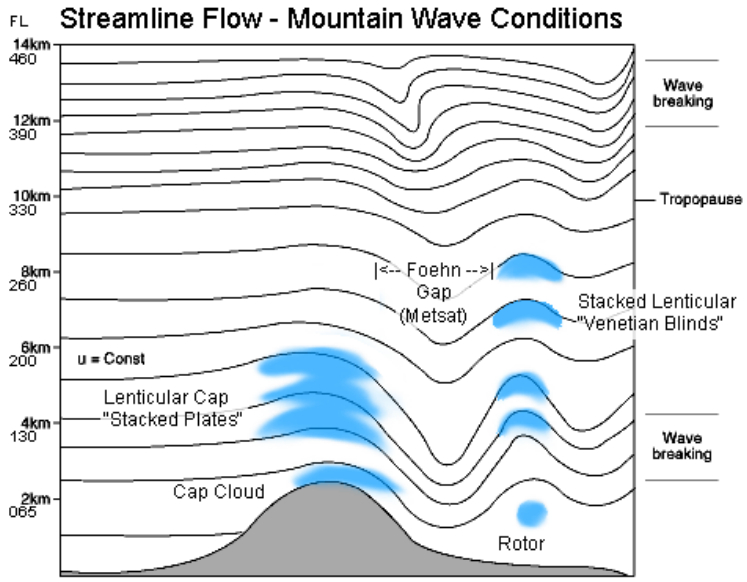

Figure 2.5 Forming of the gravity waves over mountains.
[http://www.tadpolewebworks.com/web/library/images/Mountain_GravityWave.gif]

In the troposphere, the velocity amplitudes of these waves are a few centimeters per second, but in the mesosphere they can have amplitudes of several meters per second. Their effect becomes most noticeable in the mesosphere: gravity waves dissipate energy and momentum there which influences atmospheric dynamics tremendously. A pole-to-pole circulation is unstable which results in a warm winter pole and a cold summer one, for example. Since gravity waves can propagate large distances through the atmosphere carrying energy and momentum, they contribute to the vertical coupling. It is assumed that they dominate atmospheric dynamics above 80 km height. [Houghton, 2002]

The best way of understanding the characteristics of gravity waves is to visualize a corrugated sheet moving through a fluid (see Figure 2.6).

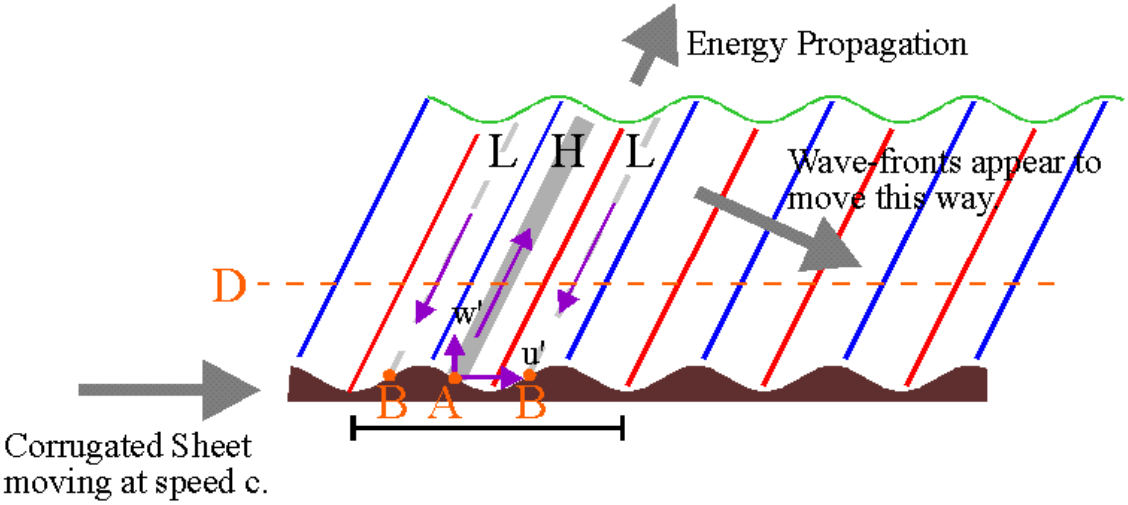

Figure 2.6 Corrugated sheet through a fluid.
[http://www.physics.uwo.ca/~whocking/p103/grav_wav.html]

At point "A", the corrugation is moving upward with increasing time, forcing the air in this region to move up and forward. Thus, the air particles will achieve a velocity component w' which is upward, and a forward component u'. This is "push" the air along the line of the purple arrow shown sloping up and to the right. As a result, the pressure is increasing along the grey line, what is a region of high pressure. The opposite holds at point "B", the corrugation is appear to be "falling away", so the air in this region will also fall. On the picture this is shown through the grey broken lines. The broken grey lines are regions of low pressure.

The vertical displacements are followed the corrugation. Parcels of air which have maximum displacement are moving along the blue lines upwards and to the right. These parcels are cooled as they rise, by adiabatic cooling, so here the wave is coldest. Parcels of air, which are shown as the red lines, propagate downwards. They are heated by adiabatic processes, and thus parcels along this line are the warmest of all.

Figure 2.7 shows how vertical displacement, velocity, pressure, and temperature vary within a buoyancy wave. The whole system appears to be stationary. A slice “D” is made through one oscillation of the wave.

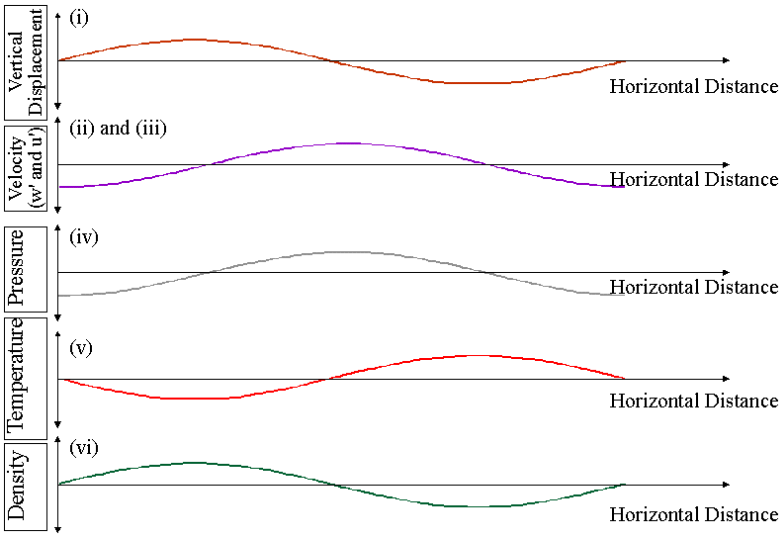

Figure 2.7 Variation of different parameters along the line D on the Figure 2.6. (i) vertical displacement, (ii) vertical velocity, (iii) horizontal velocity, (iv) pressure, (v) temperature.

Gravity waves can only exist and propagate vertically as long as the atmosphere is stable-stratified and the wave's zonal phase velocity does not equal the zonal background wind speed. Otherwise, the wave is reflected or even breaks.

The general dispersion relation for the vertical wavenumber μ_z is following:

$$\mu_z^2 = \frac{(N^2+\sigma^2)n^2}{\sigma^2-f^2} + \frac{\sigma^2}{c_s^2} + \left(\frac{N^2}{c_s^2} + E^2\right) \qquad Eq.\ 2.4$$

where $n^2=\mu_x^2+\mu_y^2$, μ_x^2 is zonal wavenumber, μ_y^2 is meridional wavenumber, N is Brunt-Vaisala frequency, σ is intrinsic rate of the wave, f is the Coriolis parameter, c_s is speed of sound, E is Eckhard coefficient. The general dispersion equation describe gravity waves, planetary waves and sound waves. In order to exclude two last mentioned let's tale next parameters $f=0$ and $c_s=\infty$. Shortened Eq. 2.4 looks following:

$$\mu_z^2 = \frac{(N^2+\sigma^2)n^2}{\sigma^2} \qquad Eq.\ 2.5$$

Given approximation is called Boussinesq approximation. If it is taken only in x-z-plane than $n^2=\mu_x^2+\mu_y^2=\mu_x^2$ and Eq. 2.5 is rewritten

$$\mu_z^2 = \frac{N^2+\sigma^2}{\sigma^2}\mu_x^2 \qquad Eq.\ 2.6$$

Taking into account next relations: $\sigma=\omega-\mu_x u_0$ (zonal background wind) and $c=\frac{\omega}{\mu_x}$ (Phase velocity in zonal direction).

$$\mu_z^2 = \frac{N^2}{(c-u_0)^2} - \mu_x^2 \qquad \textit{Eq. 2.7}$$

The Frequency of gravity wave with an assumption of $u_0=0$ becomes following:

$$\omega^2 = \frac{N^2\mu_x^2}{\mu_x^2+\mu_z^2} \qquad \textit{Eq. 2.8}$$

Because this equation related to the *x*-*z*-plane “zonal” and “horizontal” wavelength considered to be synonyms.

3. Airglow imaging

The OH airglow emission originates at near 85-90 km. In the IR spectrum emission is bright enough to be imaged by charge coupled device (CCD) cameras with exposure time from a few seconds to a few minutes. Peterson and Kieffabber (1973) were the first to show that such images of the night sky show wavelike patterns of bright and dark areas perturbing the airglow emission. Since that methods showed to be efficient, airglow imaging became a standard technique for investigation two-dimensional structures that are often present in the high altitude region over the entire night sky from horizon to horizon. Airglow imaging observations have been carried out more than 40 years for now.

3.1. Camera system

The infrared camera system, which was set by the institute, is based on the XEVA 1.7 320 USB TE3 camera from Xenics Infrared Solution company. The sensor consists of an array of photodiodes, whose absorption layer lies in the range of 0.9 - 1.7 μm of Near Infrared spectrum. The SWIRON 1.4/23 high-performance lens gives high optical imaging availability. The sensitivity range of the system itself is restricted by a long pass filter. The sensor is also protected from the sunlight by the motorized sliding cover. It also has an array cooling system which able to cooled down to 223 K in order to minimize the thermal noise impact. The working temperature is 235 K, what means that cooling works well under warm summer conditions as well.

Figure 3.1 XEVA 1.7 320 USB TE3 digital camera.

Spectral range

The output of camera represents itself a two-dimensional array of light-sensitive photodiodes in the amount of 81920, which has shape of square and laid out in 306 rows and 320 columns. The photodiodes essentially convert incident light into photoelectrons. [Jacobson et al., 2000] The signal of the light is summed for each photodiode over a certain integration time and then converts to a digital number of 12 bit data stream by using Analog-to-Digital Converter (ADC). Each pixel has a range in 12 bit, which means that values are presented from 0 to 4095. There are three parameters in Analog-to-Digital Converter (ADC Vin, ADC Vref and VDetCOM), which participate in the conversion of the signal and may affect it. ADC Vin specifies a relative value of conversion. ADC Vref determines the width of the intensity range. The intensity sensitivity of the sensor adjusts in response to incident light and can be set for the optimal contrast. VDetCOM creates a bracing on the Sensor

Substrate and also a lower extent influenced by the conversion. More detailed information is written in the manual to Xenics (2013).

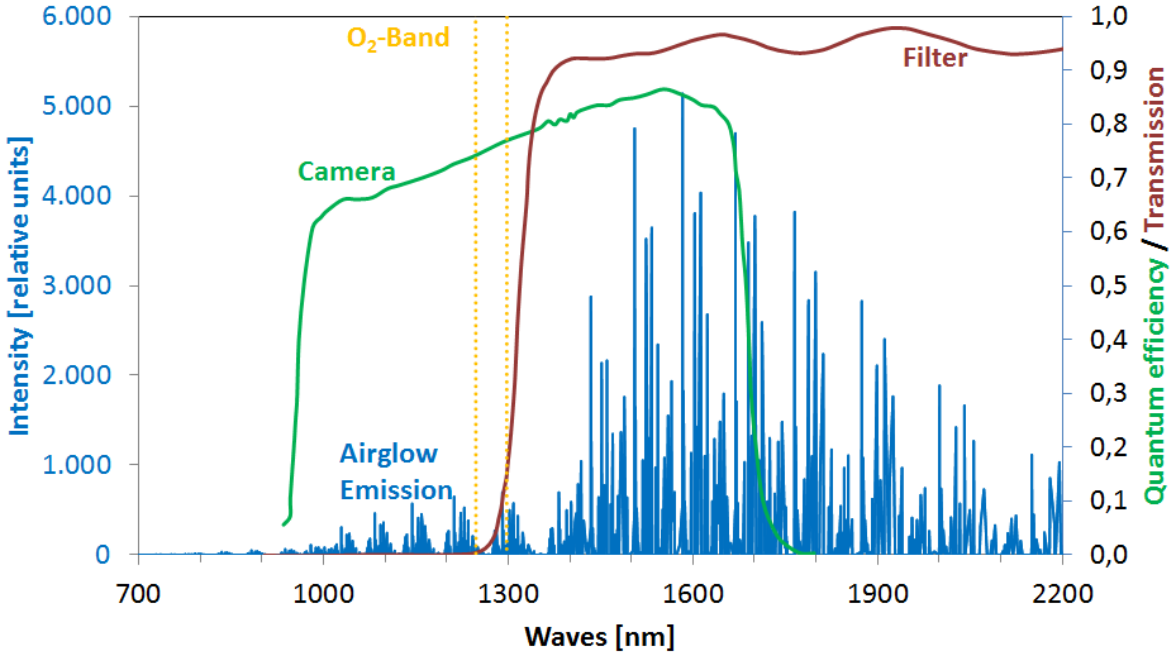

Figure 3.2 In Green: The quantum efficiency of the camera system. [Xenics (2013)] In Vinous: The transmission of long pass filter. In Blue: Transmission of the OH-airglow. [Rousselot et al., 1999] In Yellow: O_2 emission band at 1270 nm.

Quantum efficiency evaluate is the property of the material to produce the current when it is irradiated by photons of a particular wavelength. Triple semiconductor alloy InGaAS (indium gallium arsenide) is used as sensor material. Photodiodes produced by this material are in the shortwave infrared spectrum what means that they have high quantum efficiency, the camera range can be seen on the Figure 3.2. [Pearsall, 1980] The material is additionally covered with an InP (indium phosphide) substrate cover, which absorbed wavelengths below 920 nm. According to the manual the band edge of the sensor goes till 1700 nm, however, sensor is very sensitive to the temperature variations. The value can changes approximately about 8 nm per 10 ^{0}C. According to the graph sensitivity, range varies from 960 to 1640 nm at normal temperature.

The intensity distribution of airglow is shown on the figure with a blue color. It can be seen that the quantum efficiency of the camera intersects the maximum of the airglow intensity. [Rousselot et al.,1999]

O_2 emission band locates in 1270 nm. The sensitivity of camera is limited by a long-pass filter. FWHM (Full width of the half limit) is considered to be the lower limit. The recording range starts at 1320 nm and exclude the O_2 emission.

In summary, the range of OH-emission measurements with the camera lies in the near infrared spectrum from 1320 nm to 1640 nm (with filter) and from 960 nm to 1640 nm (without filter).

Recording parameters

The exposure time of the camera can be set in a wide range depending on the temperature. Currently camera produces the image every 0.5 seconds, but image is taken for every 20 seconds, because of computational time. During the work it has been proven that it is a good setting for observation of the airglow. 10 ms is required time for the processing and storage of one image. Airglow transmitted in the wide range of relative intensity amplitudes from 100 to 1000 with a maximum unit of 4095, it was done by adjusting the analog-to-digital converter parameters.

3.2. Image preprocessing

The typical example of the camera system image output can be seen on Figure 3.3 (a). The raw data is not suitable for the algorithm. Before doing an analysis some preprocessing should be done. Preprocessing of the images includes several general steps: unification of the resolution across the image, transformation of the data from the original sky format to the corresponding coordinate system, removal of stars. [Garcia et al., 1997]

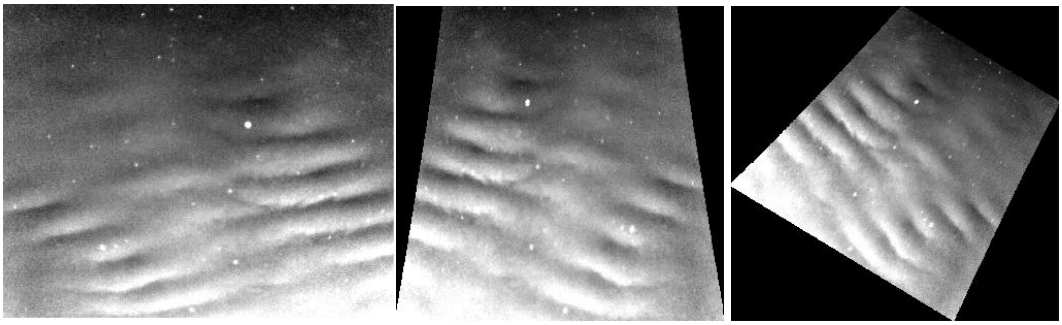

Figure 3.3 a. Raw image. b. Unified resolution image. c. Top left corner of the image has North direction.

Unification of the resolution across the image should be done, because of a quantitative analysis of the image data. It is necessary to use a coordinate system that relates distances between pixels in the image to physical distances in the airglow image.

The collimation axis of the camera is calculated from the next parameters: height of the OH-airglow layer over the surface (h) and elevation angle of the camera (γ). Because of the geometry of two parallel planes and elevation angle rectangular angle of view of the camera forms a trapezoidal section of the airglow layer. It should be taken into account, a thickness of airglow layer which is approximately 8 km and an uncertainty of ±4 km. The positon of the center of the lens is also known. The center of the lens gives the beginning of the Cartesian coordinate system x, y, z (x and y axis are located in the plane of camera parallel to the Earth surface and z- axis completes the right-handed system). Figure 3.4

gives an understanding of the geometry. Formulas for the calculation of the new form of the image are provided next.

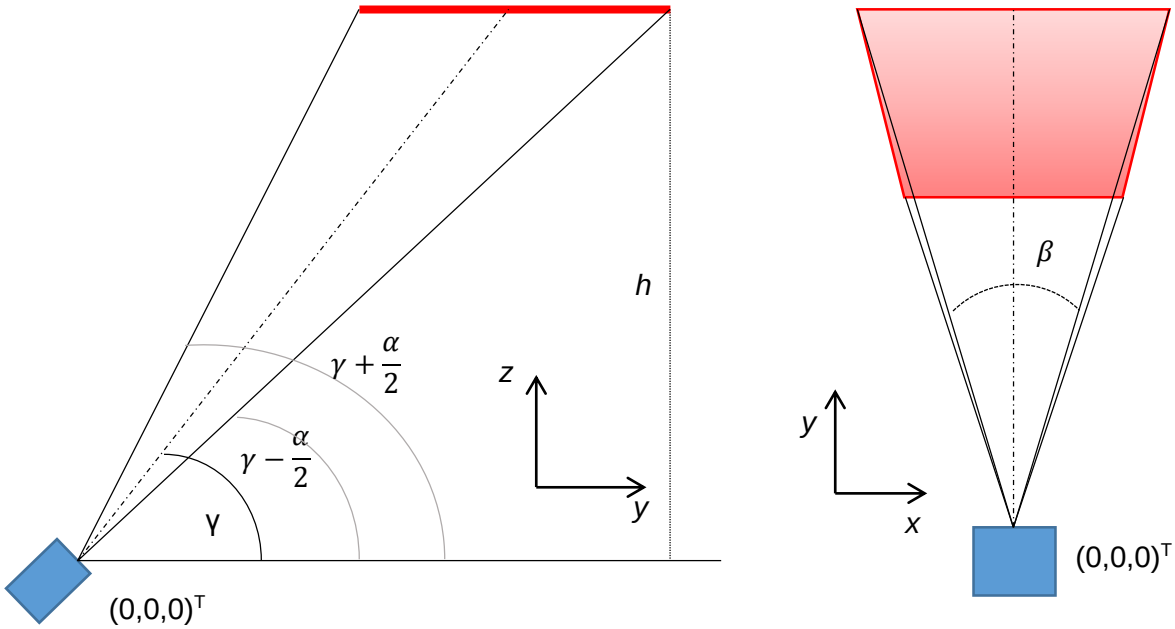

Figure 3.4 Sketch of the camera system and principal of the airglow image forming.

New points of the image are calculated with help of the Eq 3.1.

$$\begin{pmatrix} x(y(z,\theta),\theta,\varphi) \\ y(z,\theta) \\ z \end{pmatrix} = \begin{pmatrix} \sqrt{y^2+z^2}\,tan(\varphi) \\ z\,tan(90^0-\theta) \\ h = const \end{pmatrix} \qquad Eq.\ 3.1$$

where $\theta \in \left[\gamma - \frac{\alpha}{2}, \gamma + \frac{\alpha}{2}\right]$ and $\varphi \in \left[-\frac{\beta}{2}, +\frac{\beta}{2}\right]$

The maximum error is calculated with following equation, where $\Delta\theta$ and $\Delta\gamma$ are equal to 1 degree.

$$\begin{pmatrix} \Delta x \\ \Delta y \\ \Delta z \end{pmatrix} = \begin{pmatrix} \Delta y \frac{y\,tan(\varphi)}{\sqrt{y^2+z^2}} + \Delta z \frac{z\,tan(\varphi)}{\sqrt{y^2+z^2}} \\ \Delta z\ tan(90^0-\theta) + \Delta\theta \frac{z}{cos^2(90-\theta)} \\ \Delta h = const \end{pmatrix} \qquad Eq.\ 3.2$$

Bases of the trapezium are calculated next. T_B is bigger base, T_S is smaller base, T_H is height of trapezium.

$$T_B = x\left(y\left(h, \gamma - \frac{\alpha}{2}\right), h, +\frac{\beta}{2}\right) - x\left(y\left(h, \gamma - \frac{\alpha}{2}\right), h, -\frac{\beta}{2}\right) \quad Eq.\ 3.3$$

$$T_S = x\left(y\left(h, \gamma + \frac{\alpha}{2}\right), h, +\frac{\beta}{2}\right) - x\left(y\left(h, \gamma + \frac{\alpha}{2}\right), h, -\frac{\beta}{2}\right) \quad Eq.\ 3.4$$

$$T_H = y\left(h, \gamma, -\frac{\alpha}{2}\right) - y\left(h, \gamma, +\frac{\alpha}{2}\right) \quad Eq.\ 3.5$$

There are all geometrical elements that are used for the unification of the image resolution. Based on the transformation rule to each pixel in the rectangular image a new value is assigned. During this process one part of the image is compressed while another is stretched. As a result, new pixels replace old ones. On the stretched area appear some pixel's gaps, which are covered by interpolation. For the compressed area there is another problem. There are too much pixels, so the values of new pixels are calculated by taking an average value of the intensity of the new pixels. [Press et al., 1996] After this recalculation the distance of the pixels are now equivalent one to another.

In order to connect images with terrain, the image can be aligned facing north. For this purpose a two-dimensional rotational matrix is used.

$$\begin{pmatrix} x_{rot}(y(z,\theta),z,\varphi) \\ y_{rot}(z,\theta) \end{pmatrix} = \begin{bmatrix} cos(\delta) & sin(\delta) \\ -sin(\delta) & cos(\delta) \end{bmatrix} \begin{bmatrix} \sqrt{y^2 + z^2}\, tan(\varphi) \\ z\, tan(90 - \varphi) \end{bmatrix} \quad Eq.\ 3.6$$

where x_{rot} and y_{rot} are rotational coordinates and δ is angle of rotation (33^0). The result is shown on the Figure 3.3 (c). Projection of the image on the terrain can be seen on the Figure 3.5.

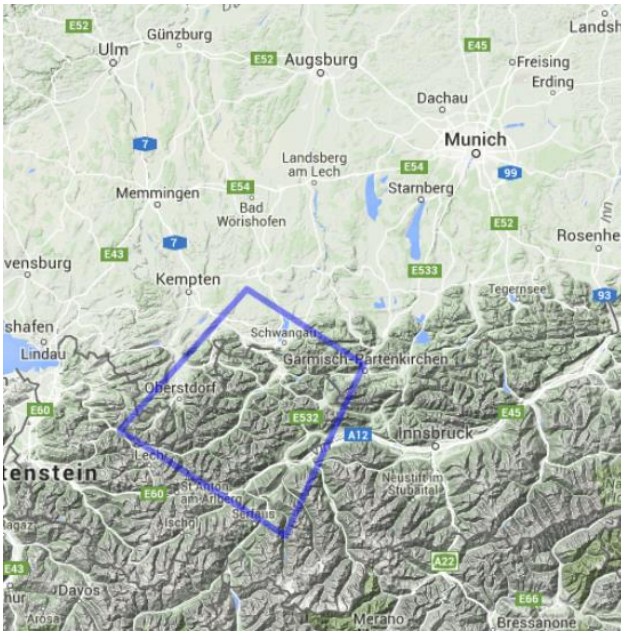

Figure 3.5 Projection of the image on the terrain. *[www.google.com/maps]*

One of the most important step is the star removal. The presence of stars on images make a big influence on the results of the algorithm. This step is one of the most difficult as

well. Going a bit ahead, let's have a look on the surface with stars and without it (see Figure 3.6). These images are shown results after detrending (description is in the chapter 4), but they show us how stars make an impact on the results. If on the image (a) we have intensity values in a range of [-80; 80] a. u. (arbitrary units) in contrary to that on the image (b) after star removal algorithm the values became more smooth and in the range of [-40; 20] a. u., what is a noticeable difference.

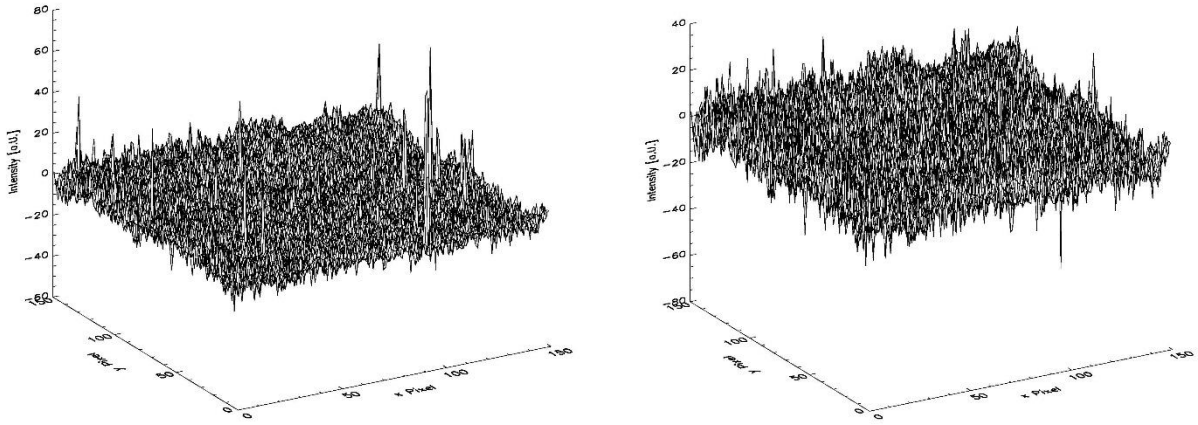

Figure 3.6 Image surface with stars (left) and without stars (right).

The short description of the star removal algorithm is next. First a Gaussian blur is defined. It is the result of blurring an image by the Gaussian function, really common effect used in the image analysis to reduce image noise and details. The results of blurring are subtracted from the original image. All values above the given threshold, which was set from the experience of working with data, are considered as stars now. For each star the maximum value in the neighbourhood is searched recursively. Now the radius of these star maxima is determined as mean value of four distances in the four main directions. Each of this radius is defined as a number of pixels till the first pixel, what value is higher than the one before. The mean radius defines all star pixels to be interpolated after their removal. Each of the star pixel is interpolated taking all surrounding pixels and excludes all other star pixels that are not inside of the cycle. The result of the star removal is given on the Figure 3.7 b and d. There are still some issues about the algorithm. In some cases it does not work perfectly. It is seen from the Figure 3.7 ab and cd pair. For ab it works perfectly no stars left, for cd it is clear that not all stars have been removed, because in consideration only bright stars are taken. The work under the star removal algorithm is still going. In the near future all limitations should be fixed.

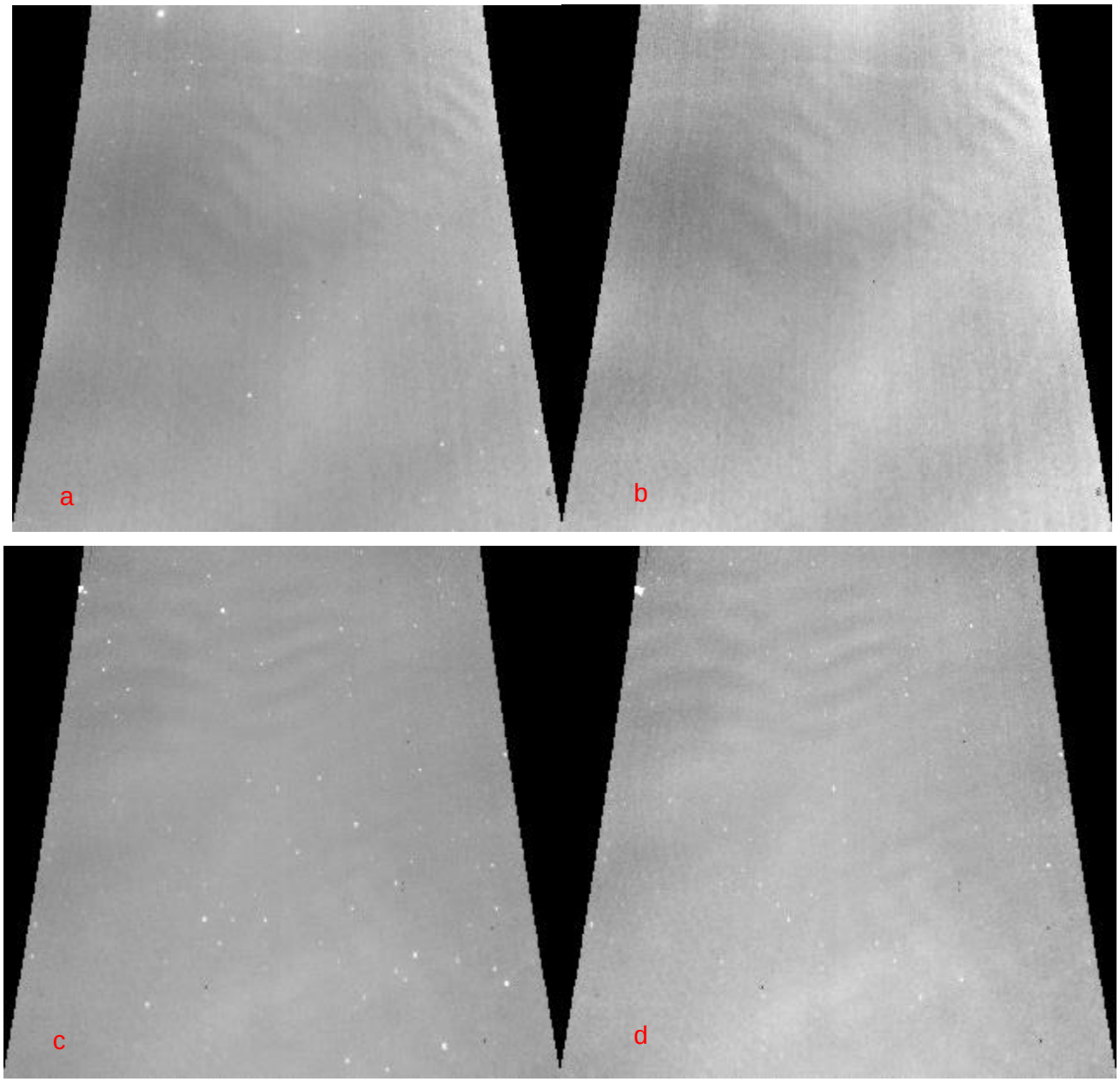

Figure 3.7 a,c. Image with stars. b,d. Image without stars.

4. Image Analysis using FFT

There is a number of tasks that are handled with Fourier techniques. Fast Fourier Transform (FFT) is the fast algorithm of the discrete Fourier transform. FFT lies at the heart of signal and image processing fields and is the main core in at the vast majority of applications. Fast Fourier Transform of the image converts image information into the frequency domain, after this process it is possible to obtain its amplitude and phase spectrum. The phase spectrum provides texture and structure information about the image and the amplitude spectrum saves contrast illumination information of the image after the decomposition. [Zhao et al., 2012] The majority of the theoretical material was taken from "Numerical recipes in C" by William H. Press et al. 2007, references for other sources will be given directly in text.

4.1. Fundamentals of FFT

4.1.1. Mathematical introduction and calculation rules

First, it will be given an introduction on the theory of the Fourier Transform. The representation of the Fourier transform can be given in the time or in the frequency domain. The common way of representation of Fourier transform equations is next:

$H(f)=\int_{-\infty}^{\infty} h(t)e^{2\pi ft}\,dt$ *Fourier Transform* *Eq. 4.1*

$h(t)=\int_{-\infty}^{\infty} H(f)e^{-2\pi ft}\,dt$ *Inverse Fourier Transform* *Eq. 4.2*

where *h(t)* is a function of time, *H(f)* is a function of frequency, with $-\infty < f < \infty$. The units of functions are dependent of each other. In our case *h* is a function of position (meters), so *H* is going to be a function of inverse wavelength (cycles per meter).

From Eq. 4.1 and Eq. 4.2 it is visible that Fourier transform is a linear operation. This basically means that the transform of the sum of two functions is equal to the sum of the transform of each function. The transform of constant times a function is that same constant times the transform of the function. Further, the following symmetry of functions hold:

Table 1 Symmetries of function in the two domain

h(t) is real	*H(-f)=*$[H(f)]$ *
h(t) is imaginary	*H(-f)=*$-[H(f)]$ *
h(t) is even	*H(-f)=H(f)* $[H(f) is\ even]$
h(t) is odd	*H(-f)=-H(f)* $[H(f) is\ odd]$
h(t) is real and even	*H(f) is real and even*
h(t) is real and odd	*H(f) is imaginary and odd*
h(t) is imaginary and even	*H(f) is imaginary and even*
h(t) is imaginary and odd	*H(f) is real and odd*

The Fourier transform has the following basic properties:

Time scaling:	$h(at) \Leftrightarrow \frac{1}{\lvert a\rvert} H\left(\frac{f}{a}\right)$	Eq. 4.3
Frequency scaling:	$\frac{1}{\lvert b\rvert} h\left(\frac{t}{b}\right) \Leftrightarrow H(bf)$	Eq. 4.4
Time shifting:	$H(t-t_0) \Leftrightarrow H(f)e^{2\pi fto}$	Eq. 4.5
Frequency shifting:	$h(t)e^{-2\pi ifto} \Leftrightarrow H(f-f_0)$	Eq. 4.6

4.1.2. Selected theorems

There exist some prominent theorems concerning the Fourier transform which are briefly summarized in the following:

Convolution theorem. It means that convolution in one domain (for example time domain) equals pointwise multiplication in the other domain. With two functions *h(t)* and *g(t)* and their corresponding Fourier transforms *H(f)* and *G(f)*. The convolution of the two functions is given by the next formula:

$g*h=\int_{-\infty}^{\infty} g(\tau)h(t-\tau)d\tau$ *Eq. 4.7*

We know that function *g*h* is a function in the time domain and has the following property *g*h=h*g*. Convolution theorem is defined by:

$g*h \Leftrightarrow G(f)H(f)$ *Eq. 4.8*

The correlation of two functions is given by next expression:

$Corr(g,h)=\int_{-\infty}^{\infty} g(\tau+t)h(\tau)d\tau$ *Eq. 4.9*

The correlation is a function of time. It is lies in the time domain and one of the transform pair. **Correlation theorem** can be written in the next manner:

$Corr(g,h) \Leftrightarrow G(f)H^*(f)$ *Eq. 4.10*

The correlation of the function with itself is called its **autocorrelation** and defined by:

$Corr(g,g) \Leftrightarrow |G(f)|^2$ *Eq. 4.11*

The total power in a signal is the same for the frequency and time domain. This property is called **Parseval's theorem**:

$Total\ Power = \int_{-\infty}^{\infty} |h(t)|^2\, dt = \int_{-\infty}^{\infty} |H(f)|^2\, df$ *Eq. 4.12*

Sampling Theorem and Aliasing

Time function *h(t)* is normally sampled into even numbers of intervals *(Δ)*. The responding of the time interval *Δ* is called sampling rate. The sampling interval determines the largest frequency which can still be resolved. This frequency is called the Niquist frequency. It is calculated using:

$f_c=\frac{1}{2\Delta}$ *Eq. 4.13*

Nyquist frequency is a half of the sampling rate of a discrete signal processing system. It is important for some of the reasons. First is known as the sampling theorem. If a continuous function *h(t)*, sampled at the interval Δ, happens to be bandwidth limited to frequencies smaller in magnitude than fc, i.e., if *H(f)=0* for all $|f| \geq f_c$, then the function *h(t)* is completely determined by its samples h_n. In fact, *h(t)* is given by the formula

$h(t)= \Delta\sum_{n=-\infty}^{+\infty} h_n \frac{sin[2\pi f_c(t-n\Delta)]}{\pi(t-n\Delta)}$ *Eq. 4.14*

This theorem shows that the “information content” of a bandwidth limited function is infinitely smaller than that of a general continuous function.

However discrete sampling leads to aliasing. All of the power spectral density that lies outside the frequency range $-f_c < f < f_c$ is moved into this range. One possible step to avoid aliasing is to sample at a rate sufficiently rapid to give at least two points per cycle of the highest frequency present. This is only possible if the highest frequency is known or can be estimated. Figure 4.1 illustrates these consideration. Part (a) shows a continuous function which is nonzero only for a finite interval of time *T*. Its Fourier transform is shown schematically in (b), it is not bandwidth limited but has finite amplitude for all frequencies. If the original function is sampled with a sampling interval Δ (part (a)), then the Fourier transform (c) is defined only between plus and minus the Nyquist critical frequency. Power outside that range is folded over (“aliased”) into the range.

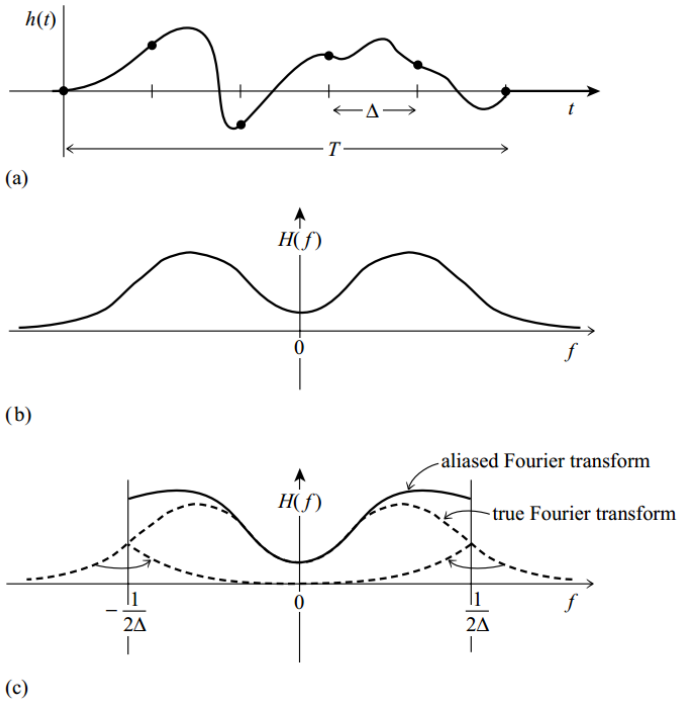

Figure 4.1 Continuous function and Sketch of the Fourier transform. [Press et al., 1996]

4.1.3. Discrete Fourier Transform

Assume that there is a sampling interval Δ. N is even consecutive sampled values. h_k is the function of which the FT will be calculated

$h_k=h(t_k), \quad t_k=k\Delta,\ k=0,\ 1,\ 2,\ldots\ldots,\ N-1$ *Eq. 4.15*

The estimation of the Fourier transform $H(f)$ will be done only for discrete values. The extreme values of n correspond to the lower and upper limits of the Nyquist frequency range.

$f_n=\frac{n}{N\Delta},\ n=-\frac{N}{2},\ \ldots,\ \frac{N}{2}$ *Eq. 4.16*

The discrete Fourier transform H_n is then defined as

$H_n \equiv \sum_{k=0}^{N-1} h_k\, e^{2\pi i k n/N}$ *Eq. 4.17*

It can be added that the discrete Fourier transform does not depend on the time scale Δ. It has almost exactly the same symmetry properties as the continuous Fourier transform. (see Table 1)

The formula for the discrete inverse Fourier transform is given by the Eq. 4.18.

$h_k=\frac{1}{N}\sum_{k=0}^{N-1} H_n\, e^{-2\pi i k n/N}$ *Eq. 4.18*

4.1.4. Fast Fourier Transform

The FFT is an algorithm that computes the discrete Fourier transform of a sequence or its inverse. Since N can be rather large with the discrete Fourier transform can become a tough task. In 1965, Cooley and Turkey rediscovered (it was previously used by Gauss and Runge) a very efficient way of calculating the discrete Fourier transform known as the Fast Fourier Transform.

There are many varieties of the FFT algorithm; here only the simplest form, named decimation in time algorithm, which has been used for the realization of the FFT function for the IDL, will be described.

W is defined as a complex number

$$W=e^{2\pi i/N} \qquad \textit{Eq. 4.19}$$

Eq. 4.17 can be written as

$$H_n=\sum_{k=0}^{N-1} W^{nk} h_k \qquad \textit{Eq. 4.20}$$

The vector h_k is multiplied by a matrix whose *(n, k)* element is the constant *W* to the power *n×k*. The matrix multiplication produces a vector results whose components are the H_n. This matrix multiplication requires N^2 complex multiplications. In addition a smaller number of operations is needed to generate the required powers of *W*. The discrete Fourier transform is an $O(N^2)$ process, but it also can be computed in $O(N \log_2 N)$ operations with the FFT.

The Fourier transform of length *N* can be rewritten as the sum of two discrete Fourier transforms, each are of length *N/2*:

$$\begin{aligned} F_k &= \sum_{j=0}^{N-1} e^{2\pi ijk/N} h_j \\ &= \sum_{j=0}^{N/2-1} e^{2\pi ik(2j)/N} h_{2j} + \sum_{j=0}^{N/2-1} e^{2\pi ik(2j+1)/N} h_{2j+1} \\ &= \underbrace{\sum_{j=0}^{N/2-1} e^{2\pi ikj/(N/2)} h_{2j}}_{F_k^e} + W^k \underbrace{\sum_{j=0}^{N/2-1} e^{2\pi ikj/(N/2)} h_{2j+1}}_{F_k^0} \end{aligned} \qquad \textit{Eq. 4.21}$$

F_k^e defines the *k*th component of the Fourier transform of the length *N/2* formed from the even components of the original f_j, while F_k^0 is the corresponding transform of length *N/2* formed from the odd components. The transforms F_k^e and F_k^0 are periodic in *k* with length *N/2*. This all was proven by Danielson and Lanczos in 1942.

Here is given the structure of the FFT algorithm. It has two sections. The first section sorts the data into bit-reversed order. This does not take additional storage. The second section executes $\log_2 N$ times included an outer loop and calculates transforms of length 2, 4, 8, …, *N*. For each stage of this process, two nested inner loops (for odd and even

components, see Eq. 4.21) are carried out which are based on range over the subtransforms already computed. The recursive computation of the FFT and of the Eq. 4.21 save computing time.

It should be also mentioned that there exists a number of other FFT implementations. The algorithm described above first rearranges the input elements into bit-reverse order and then computes the output transform in log_2N iterations. This sequence is called a decimation in time, as it was already mentioned before, or Cooley-Turkey FFT algorithm. If it is for example organized the opposite way: it is called decimation in frequency or Sande-Turkey FFT algorithm.

4.1.5. Data Windowing

The input data is considered to be periodic, but in reality it is not true. When the FFT algorithm is applied to data which is not exactly periodic the so called leakage effect occurs. Leakage is the smudging energy from the true frequency of the signal into adjacent frequencies. It also influences on the amplitude representation of the signal and makes the value smaller than they should be. [Hartmann, 1997] The example of periodic and non-periodic signal and its effect on the FFT can be seen on Figure 4.2. The frequency content of the signal is spread over adjacent frequencies when the signal is not periodic.

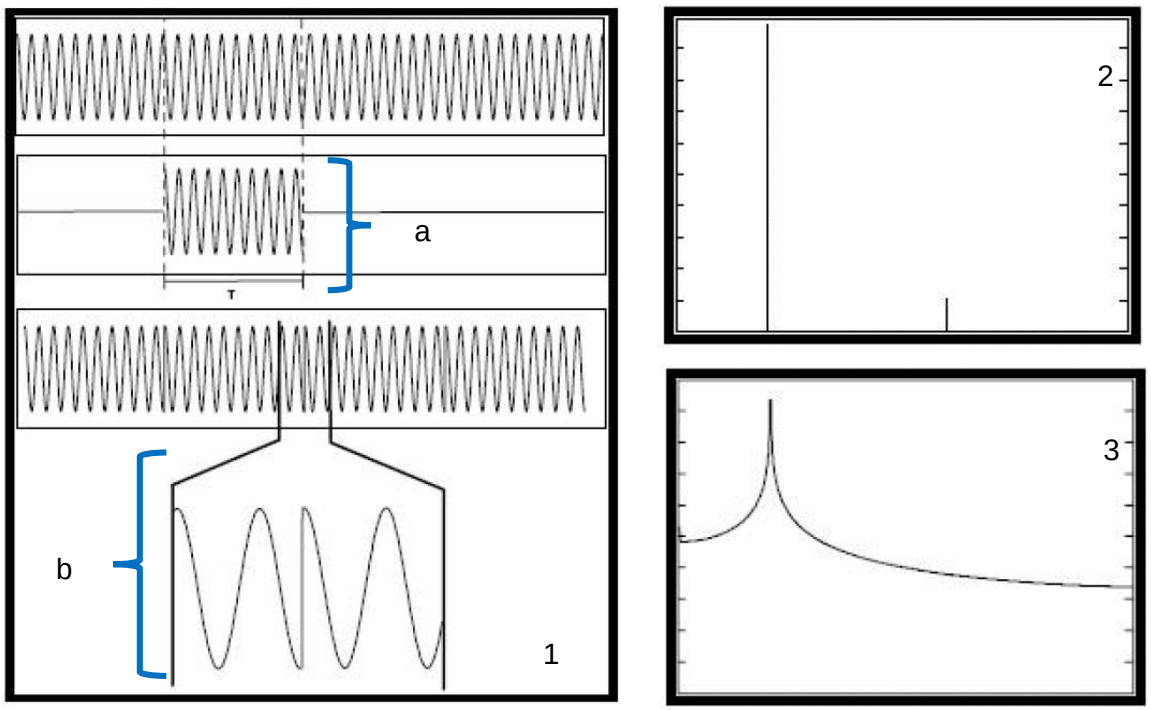

Figure 4.2 1: Example of Periodic (a) and Non-periodic (b) signal. 2: FFT of periodic signal. 3: FFT of Non-periodic signal.

To get rid of the leakage effect an appropriate window function should be applied. There are various windowing functions with their strength and weaknesses like: Blackman, Flat top, Hanning, Hamming, Welch ect. The best type of window should be chosen for each specific application carefully. [Hartmann, 1997]

Let us have more precise look on the windowing process. The window function, as a function of *s* (s is independent variable) the frequency offset in bins looks next:

$$W(s)= \frac{1}{N^2}\left[\frac{sin(\pi s)}{sin\left(\frac{\pi s}{N}\right)}\right]^2 \qquad Eq.\ 4.22$$

where *N* is sampled points. Here should be taken into account that *W(s)* has oscillatory lobes, but fall-off is not a very rapid. It can be also admitted that *W(s)* happens to be zero for *s* equal to a nonzero integer. The idea of data windowing is to modify Eq. 4.22. The function expresses the relation between the spectral estimate at a discrete frequency and the actual underlying continuous spectrum at nearby frequency. The data in general are windowed by a square window function. Determination of Eq. 4.22 goes as the square of the discrete Fourier transform of the unity window function.

$$W(s) = \frac{1}{N^2}\left[\frac{sin(\pi s)}{sin\left(\frac{\pi s}{N}\right)}\right]^2 = \frac{1}{N^2}\left|\sum_{k=0}^{N-1} e^{2\pi isk/N}\right|^2 \qquad Eq.\ 4.23$$

The reason for the leakage for the large values of *s*, is that the square window function turns on and off so rapidly. To escape this situation the input data can be multiplied by a window function w_j that changes more gradually from zero to a maximum and then back to zero. Where W_{ss} stands for “window squared and summed”:

$$W_{ss} \equiv N\sum_{j=0}^{N-1} wj^2 \qquad Eq.\ 4.24$$

More general form of the equation Eq. 4.22 can be given in terms of the window function:

$$W(s) = \frac{1}{W_{ss}}\left|\sum_{k=0}^{N-1} e^{2\pi isk/N}\right|^2 \qquad Eq.\ 4.25$$

Many different windows are existing, each of this functions have its own advantages and disadvantages. One of the window type is so called the “Rectangular” window; it does not weight the signal and it is possible to say that window was used. It is good for signals that satisfy the periodicity requirement of the FFT process and frequency resolution is important. The next group is the “Flat Top” window which is used in the case of signal amplitude importance, but it has poor frequency resolution so that the exact frequency content may be hard to determine. [Hartmann, 1997]

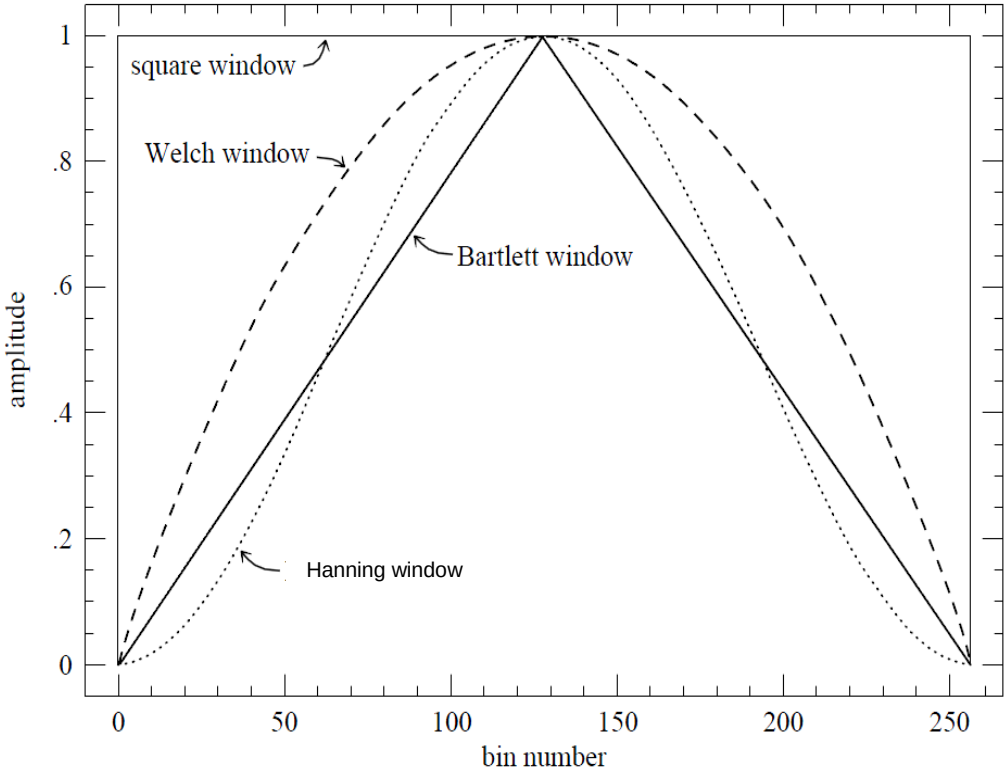

Figure 4.3 Window functions used in FFT power spectral estimation. [Press et al., 1992]

The most suitable window for the data set used in this work is the Hanning window. The Hanning window has following features: it is good for random type of signal and provides a good frequency resolution and amplitude accuracy. [Hartmann, 1997] The equation of the Hanning window looks next:

$$w_j = \frac{1}{2}\left[1 - cos\left(\frac{2\pi j}{N}\right)\right] \qquad Eq.\ 4.26$$

The Hanning window is a balance between the Flat Top and Rectangular windows. It helps to keep stable the amplitude of the signal and save the frequency resolution.

4.1.6. Two Dimensional Fast Fourier Transform

For a given complex function $h(k_1, k_2)$ defined over the two dimensional grid $0 \leq k_1 \leq N_1-1$, $0 \leq k_2 \leq N_2-1$, it is possible to calculate 2D FFT:

$$H(n_1, n_2) = \sum_{k_2=0}^{N_2-1} \sum_{k_1=0}^{N_1-1} exp(2\pi i k_2 n_2/N_2)\, exp(2\pi i k_1 n_1/N_1)\, h(k_1, k_2) \qquad Eq.\ 4.27$$

In general, the two dimensional FFT can be computed by taking one dimensional FFT sequentially on each index of the original function. Most features of the two dimensional FFT are the same as in the one dimensional case:

- Frequencies for each separate dimension are arranged in wrap-around order in the transform.
- The input data are also treated as if they were wrapped around.
- For spatial filtering in order to escape wrap-around effect, the border of multidimensional array should be zero-pad
- Aliasing effect should be taken into account, that is why should be chosen sufficient bandwidth limiting.

Two dimensional FFT is particularly important in the field of image processing. An image is usually represented as a two dimensional array of pixel intensities. There are a number of mathematical operations that can be done over the image: filtering of high or low frequency spatial components, convolve or disconvolve the image. The FFT is truly the most efficient technique in the field of image analysis.

4.2. Processing airglow images with the FFT algorithm

In this master thesis, the results of a 2D-FFT applied on airglow images are shown. The main steps which are necessary to prepare the images for a 2D-FFT and which are used to extract the most important information afterwards are sketched in Figure 4.4. They are explained in details in the following subsections.

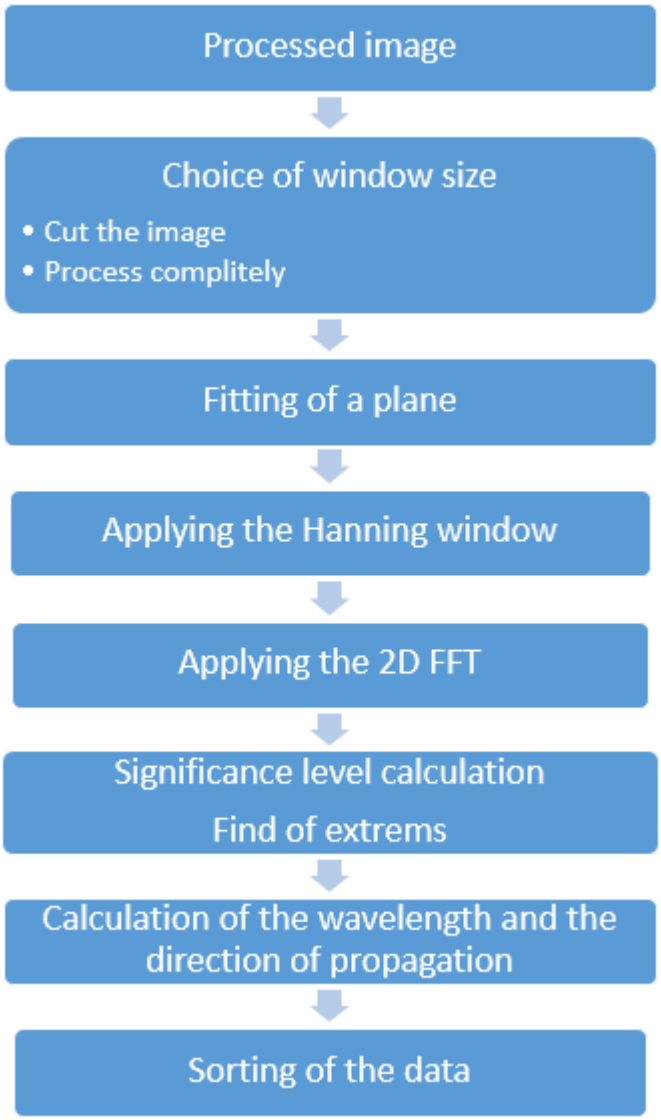

Figure 4.4 Process flow chart.

4.2.1. Preparation of data

An experimental data is never given as a continuous function, normally it is given as discrete data (samples). The input data in this case are processed sky images. Image preprocessing includes steps that were explained in the chapter 3.

Windowing of the image

The main interest of this work is in smaller-scale waves (5-20 km). As already mentioned before, the size of the image is 61x64 km. For the purpose of detection of smaller wave forms (till 15km), the image is divided into smaller windows of size 150x150 pixels, or 30x30 km. The location of the windows across the image can be seen in the Figure 4.5.

For every window the same steps of the algorithm are applied. In order to analyze also waves with horizontal wavelengths large than 15 km FFT, the algorithm is applied to the whole image without cutting. Black triangles on the top of the image are excluded from the process of the analyses, because they might have an impact on the results.

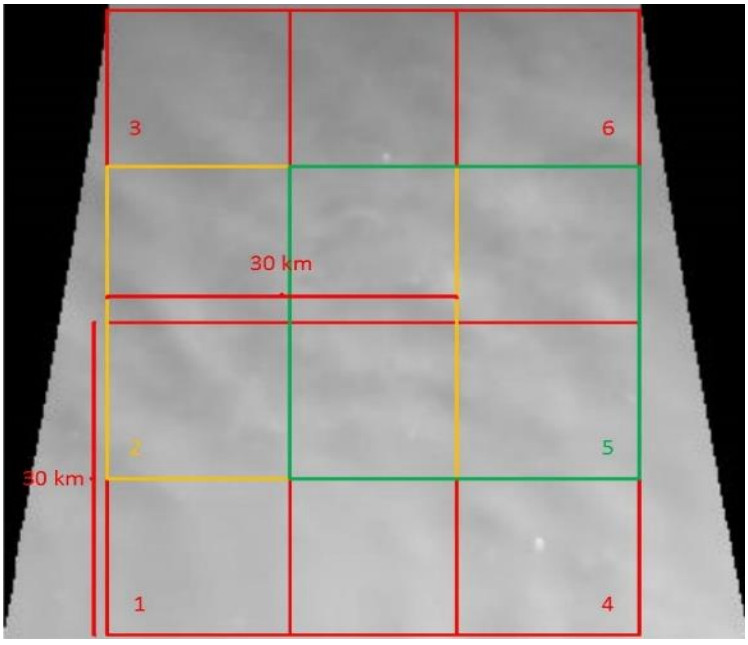

Figure 4.5 Windowing of the image.

Fitting a plane

The first step is to remove linear trends associated with gradual variations in amplitude spectrum across the field of view in order to create well-defined peaks in the transform. For this purpose we are fitting a plane to the image and then subtracting it. [Garcia et al., 1997] The other reason for detrending data is the van Rhijn Effect.

The fitting plane is created by the SFIT routine in IDL. The SFIT function determines a polynomial fit to a surface and returns a fitted array. The fitted function is:

$$f(x,y)=\sum kx_{j,i} * x^i * y^j \qquad \textit{Eq. 4.28}$$

The maximum degree of fit was chosen 4. Figure 4.6 gives an idea of how a fitting surface of degree 4 looks like. [Exelis Visual Information Solutions]

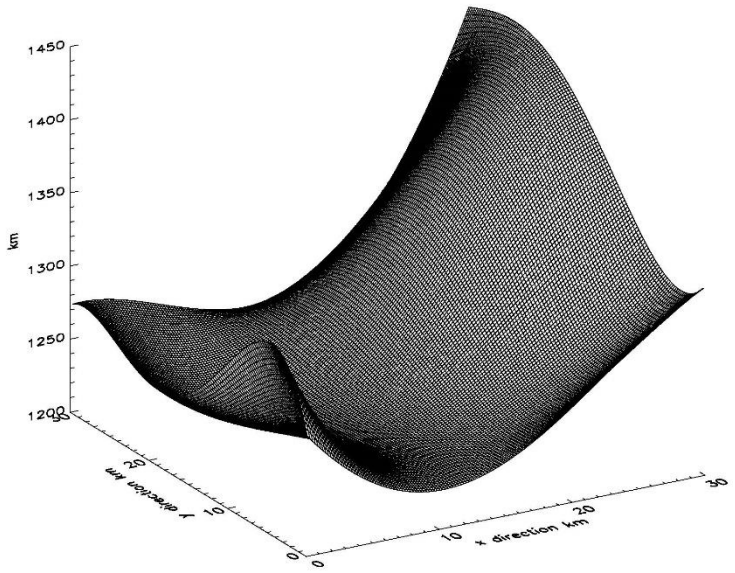

Figure 4.6 Fitting surface with degree of fit 4.

Further examples of application of a fitting surface are given. Figure 4.7 shows the real data. The Figure 4.8 shows the result of the subtraction of the fitting surface from the real data. The data now oscillate around zero.

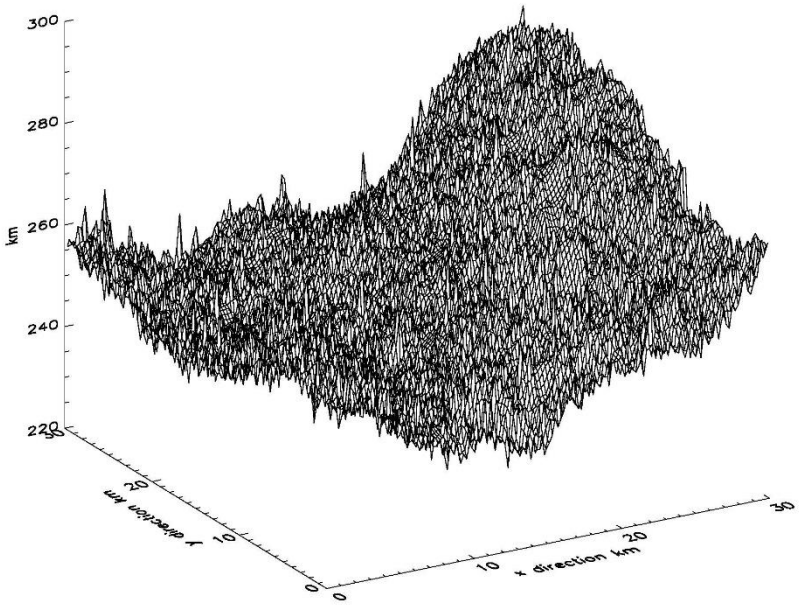

Figure 4.7 Real data representation.

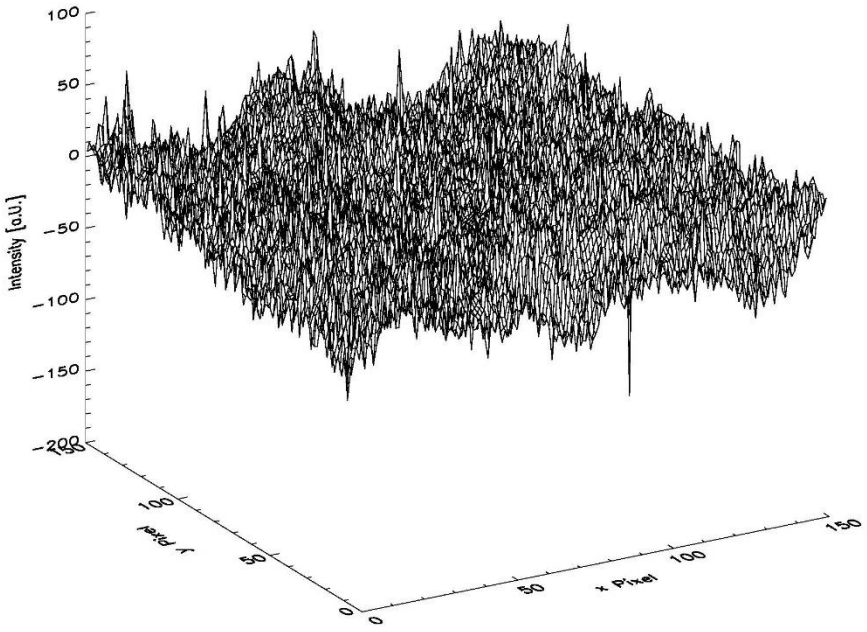

Figure 4.8 Results of the fitting surface.

Windowing

The Hanning window is chosen for the data set, because of it presents a good balance keeping the amplitude of the signal stable and saving the frequency resolution. Another important reason is the origin of the data, which are a random type of signal. To get an idea how the Hanning window looks like applied on the real data set, look at Figure 4.9.

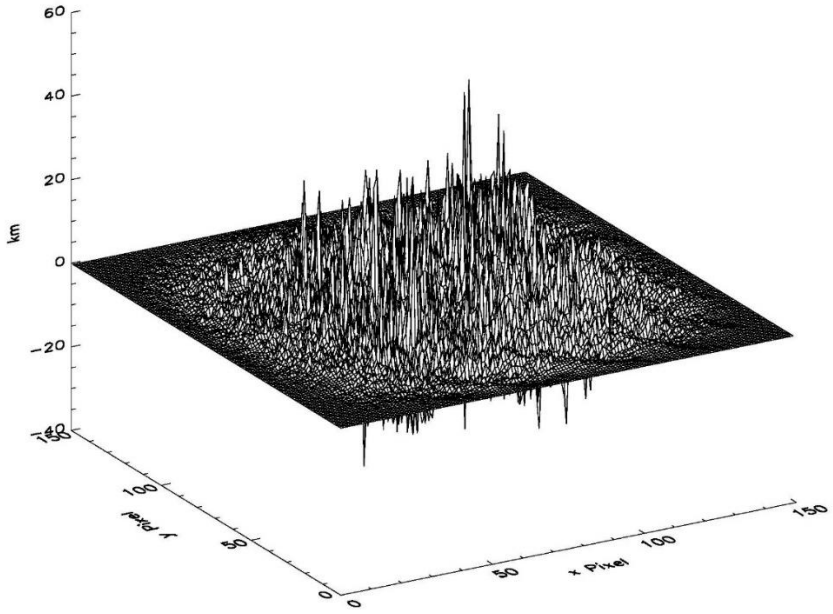

Figure 4.9 The Hanning window.

Figure 4.9 shows that the surface took a convex form.

4.2.2. Application of 2D-FFT

Now, the 2D FFT is applied to the picture. As already mentioned before, the Fast Fourier Transform is commonly used to transform an image between the spatial and frequency domain. In the frequency domain, pixel location is represented by its x- and y-frequencies and its value is named by amplitude. The FFT function decomposes an image into sines and cosines of varying amplitudes and phases, which reveals repeating patterns within the image.

Low frequencies contain the most significant information and determine the overall shape or pattern in the image. High frequencies provide more detail information about the image but contain more noise. When using forward FFT, the lowest frequencies are often shown by a large peak in the center of the data. Figure 4.10 shows the results of the FFT function plotted as a surface, with the origin (0, 0) of the x- and y-frequencies shifted to the

center. Figure 4.11 represents results of the FFT in 2D. [Exelis Visual Information Solutions] Frequency of the magnitude then increases with distance from the origin:

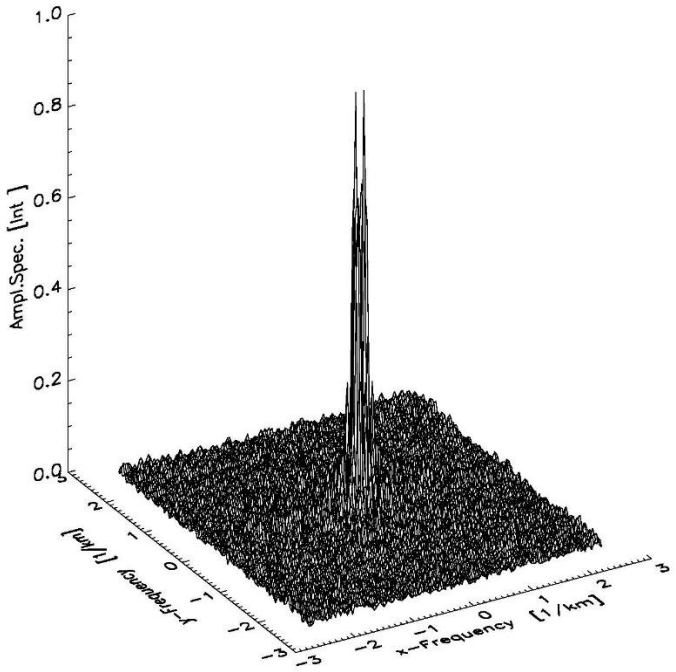

Figure 4.10 FFT surface.

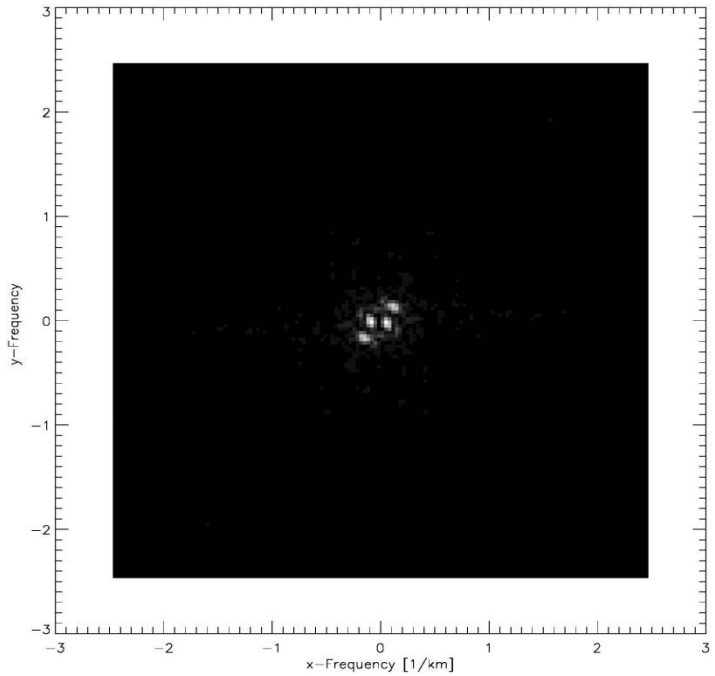

Figure 4.11 2D FFT representation.

The range of values from the low-frequency peak to the high-frequency consists from extremes. This leads to the next step of the analysis process. The most significant maximums on the region of interests should be found. In order to identify significant peaks only, a significance test is applied. First thing that should be done is finding of the significance level and cutting of the all high-frequency surface that locates beneath significance level. Significance level or alpha level itself is the probability of rejecting the null hypothesis given that it is true. By convention, the significance level is set to 0.05 (5%), implying that it is acceptable to have a 5% probability rejecting the null hypothesis. [Craparo, 2007] Random data (*N* (0, 1) – distributed) are generated. Through the addition of the mean and the multiplication with the standard deviation of the real data and division with the standard deviation of the random data. (see Eq. 4.29) The distribution of the random data is adapted to the distribution of the real data.

$$Random\_field=(M+R_m)\,\sigma(M)/\sigma(R_m) \qquad Eq.\ 4.29$$

where M is a mean value of the real data, R_m is a matrix of random generated values and $\sigma(R_m)$ is standard deviation of the random data, $\sigma(M)$ is the standard deviation of the real numbers.

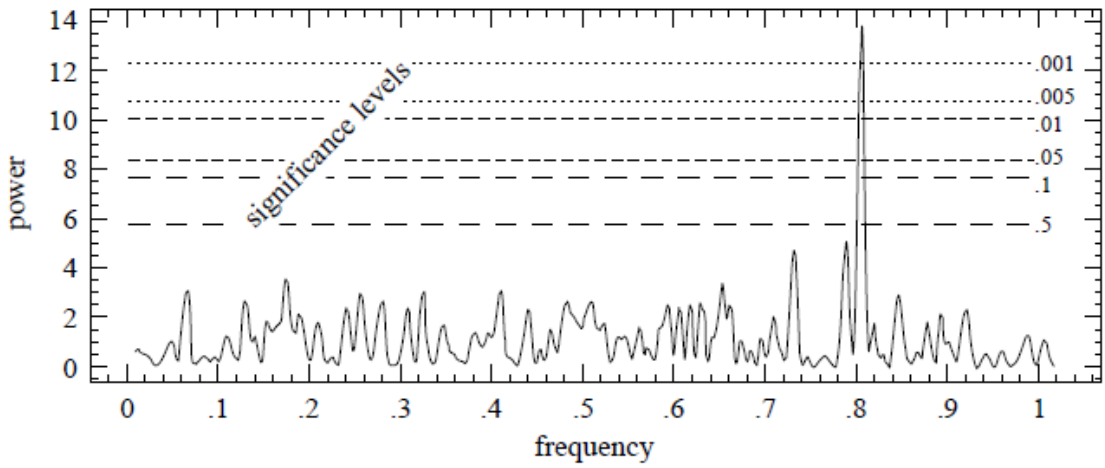

Figure 4.12 Significant level. [Press et al.,1996]

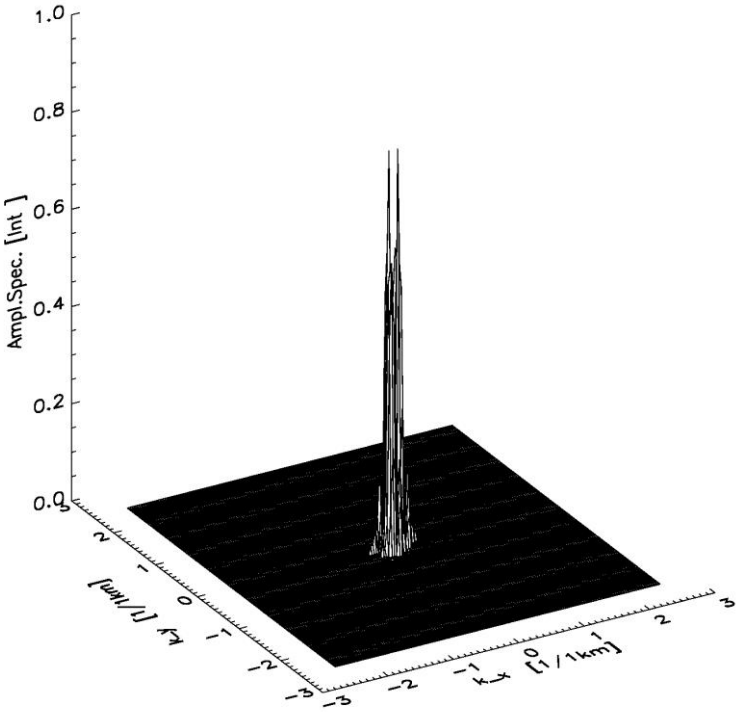

Figure 4.13 Significant peaks from the FFT surface.

Figure 4.12 gives an overview of the idea of the significance level. Figure 4.13 shows the result of the subtraction of the significance level from the FFT surface. This figure shows us the most significant peaks of the surface. Peaks contain the information that we are looking for. There is an assumption that from each area of interests it is possible to estimate by sight from the area three waveforms maximum. So the algorithm is looking only for three most significant maximums.

Maximums are defined with a help of EXTEREMES_2D function, which is installed in IDL. This function finds local extremes in a 2-d array of the image. Maxima are sorted in descending order of value what makes easy to eliminate the rest.

After finding the maxima, it is possible to calculate wavelength and angle of propagation:

$$Wavelength = \frac{1}{\sqrt{frequency\_x^2 + frequency\_y^2}} \qquad Eq.\ 4.30$$

$$Angle = atan\left(\frac{frequency\_y}{frequency\_x}\right) \qquad Eq.\ 4.31$$

where frequency-x/ frequency-y is the frequency in x-/ y- direction of a significant peak in the FFT spectrum.

4.2.3. Sorting

After applying the windowed 2D-FFT to all images taken during one night there is a big amount of data. Due to overlapping of the different windows (see Figure 4.5) and a sampling rate of the image per 20 seconds, there are a lot of repeats of the same waveforms in the output data. To free the output data from these repeats at least in parts one wave form was only counted and analyzed once for every image even if it was deleted more than once in the whole image. It basically means that all wave structures with the same wavelength and angle of propagation in the same image are deleted.

Due to different reasons the 2D-FFT results still contain artificial signals (see Figure 4.14), have to be neglected. Table 2 shows their wavelength and propagation angles. Results with these characteristics are deleted.

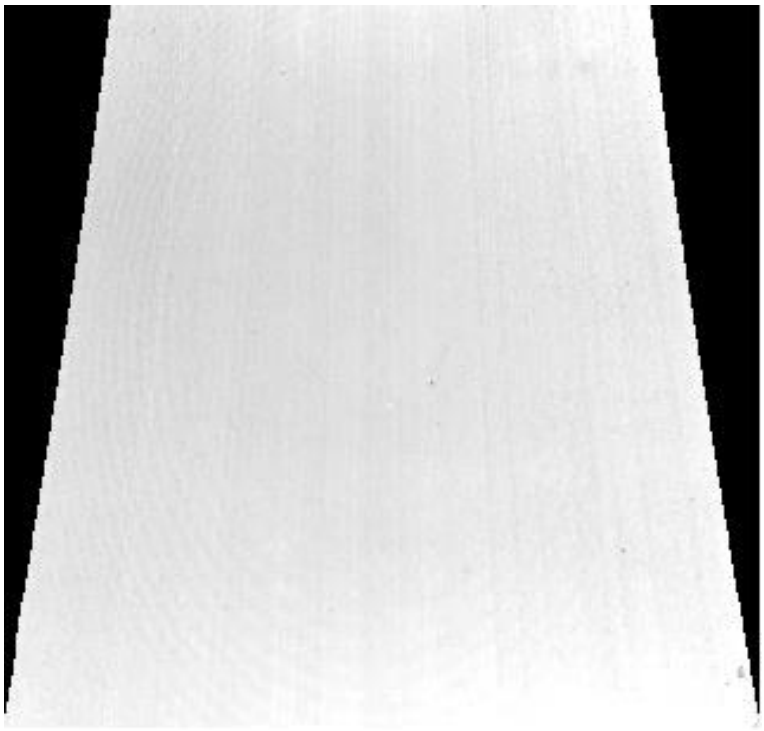

Figure 4.14 Noise.

The reason of the cycles is aberration and for stripes it is fixed-pattern noise (FPN). Aberration is an optical effect occurring in lens of the camera due to the increased reflection of light rays when they strike a lens or a reflection of light rays when they strike a mirror near its edge. Fixed pattern noise is a particular noise pattern on digital imaging sensors due to long exposure shots where particular pixels are susceptible to giving brighter intensities above the general background noise. FPN is commonly suppressed by flat-field correction. FPN is always present and constant with fixed temperature and others settings. Values are might be higher with higher exposer time. It is very important that this correction usually is very sensitive to modifications of the system parameters (exposure time, temperature etc.). The main challenge is to generate a flat field illumination for short time exposures and wavelengths. Aberration depends on many factors and can’t be fixed in the same way for all

of the images. The idea is that calibration of the equipment is time consuming process. The system itself was built on the January of 2014. The first half of the year is highly influenced by the inaccuracy of the calibration. Last five months have better realization, but there is still some work to be done on the removal of noise from the images.

Table 2 Results of the noisy image.

Wavelength	Angle of propagation
5,0000001	0
0,80962888	3,094058
1,0338683	1,974934
1,2489164	2,385944
3,7500001	0
6,0000001	0
1,3622298	2,6025621
7,5000001	0
1,4981285	-2,8624051
1,6641006	-3,17983
1,9955703	-3,8140747
10	0

An improved the camera calibration can enhance the results, but this is still in the process.

5. Results

5.1. Waves with wavelength smaller than 15 km

The camera system was collecting data during the whole year 2014. Due of some calibration and technical issues, as mentioned in the chapter 3, just 6 month from July till December are analyzed. The data for all of the nights is sorted out from clouds and moon appearance. The total number of wave events during clear sky is 323 828. This number varies from month to month. The biggest amount of waves is observed during September and equal to 74 343 wave events. The smallest one can be registered during December (32732).

Figure 5.1 displays the distribution of the observed wave events with horizontal wavelength of up to 15 km. The maximum horizontal wavelength is due to the window size of 30x30 km as described in chapter 2. The results are given in the percentage equivalent to the total numbers of wave events per month. The bin size of the histogram is 2 km. The smallest waves (horizontal wavelength till 2 km) are barely found. Its frequency of occurrence ranges about 1%. There is almost none of them during July (0.1%), but in comparison to it, December gives decent amount of 4.5%. Waves from 2-4 km start from 11% in July and increase their presence till 16% in September and then slowly decrease their number till the end of the year. The biggest proportion belongs to the waves in the range 4-6 km. The percentage is around 33% +/- 2%, with the highest 35% in September. Its presence decreases dramatically only in December till the value of 27%. Waves range of 6-8 km stay stable around 12%. Waves in a range 8-10 km have the second biggest proportion of presence. Summer months have 19% from the total number of waves. From September till November the range increases from 16 till 20%. December has 18%. In September the percentage equal to the percentage of waves with size 2-4 km. The next bin refers with a horizontal wavelength of 10-12 km. This range has one of the smallest numbers of appearance during the whole time of the observations. September has 6% from the total amount. December has 8% and the others months are 7%. The last bin (12-14 km) is almost twice as much as previous one. The values range from 15.5% until 16.5% and in December it is 19%. Wave events with horizontal wavelengths between 12 km and 14 km are identified about twice as much as waves with horizontal wavelength of 10 km to 12 km.

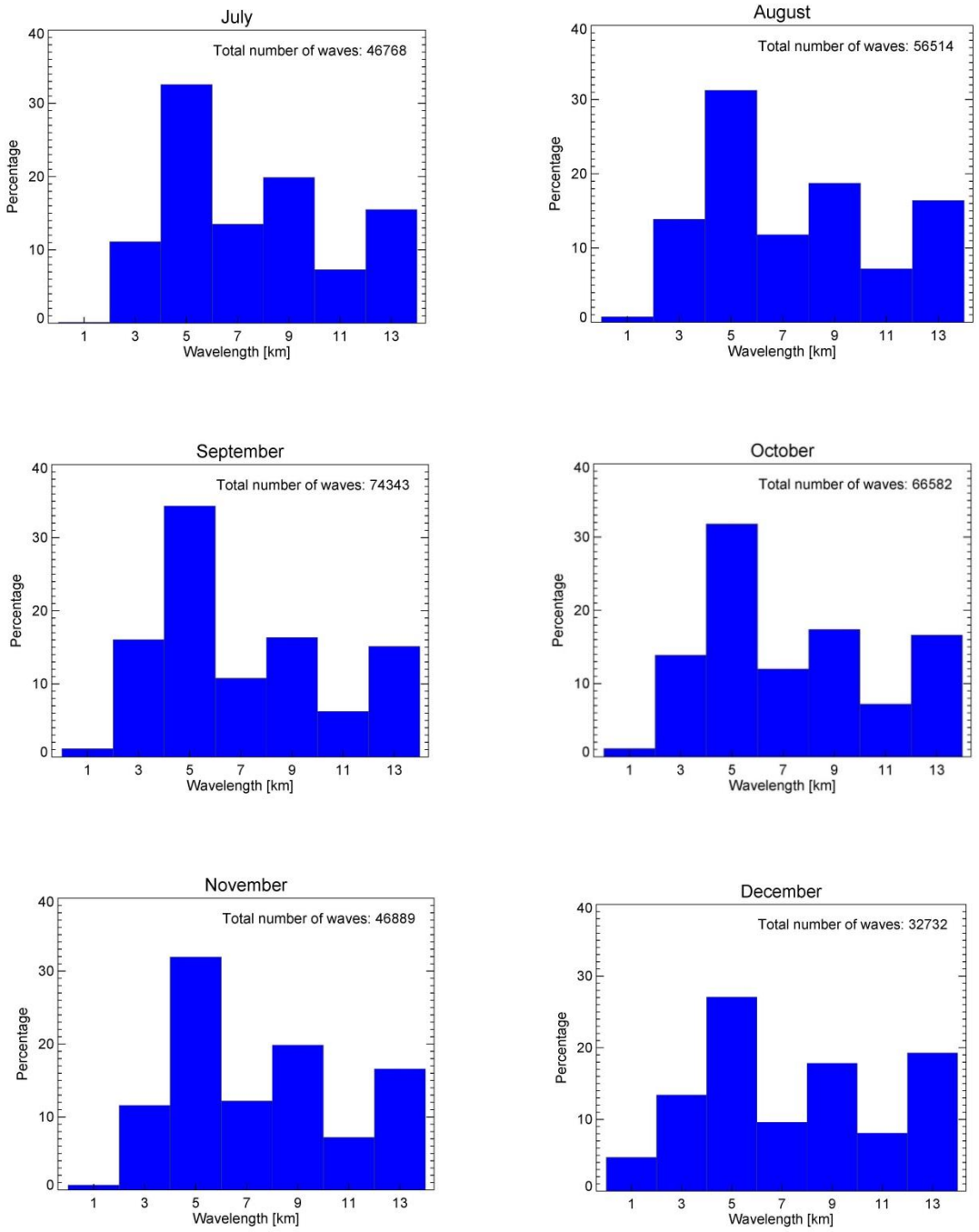

Figure 5.1 Histograms of the occurrence of gravity waves events during the observatoin period from July till December with maximum wavelength of 15 km.

First of all it should be mentioned that angles are given in the image coordinate system. It means that a direction of 0 degree is equal to the x axis of the image. Figure 5.2 shows the direction of the wave propagation. The bin size is chosen to be 20 degrees. The results are given in percentage of the total amount of wave events per month as in Figure 5.1. The distribution of the propagation directions is symmetric to 0 degree. First it can be seen that the bin in the range from -10^0 to 10^0 degrees has one of the smallest value during the whole observation time. In July it starts with 7 % and continues to rise. In August it is 8%, in September the percentage rises till 12%, after that it falls till 7% again in November. December shows the highest value of 17%. Bins with ranges [-30^0, -10^0] and [10^0, 30^0] have approximately the same distribution over all months with the highest value of ca. 17%, the difference reaches 2% at maximum in December. The second pair is with a propagation direction of [-50^0, -30^0] and [30^0, 50^0]. In July [-50^0, -30^0] bin is equal 13%, [30^0, 50^0] bin's value is 12%. In August and October difference is opposite, [-50^0, -30^0] bin is smaller than [30^0, 50^0] for about 1.5% in both cases. In September and November there is no difference between the pairs and values are 11% for these two months. December has unique values: [-50^0, -30^0] bin is 8.5% and [30^0, 50^0] bin is 12.5%. The next bin pair [-70^0, -50^0] and [50^0, 70^0] reaches absolute values of around 11% with slight variations of 0.5%. In December [-70^0, -50^0] has 9% and [-50^0, -70^0] has 12.5%. The last pair is [-90^0, -70^0] and [70^0, 90^0]. It has the lowest frequency of occurrence and varies from 6.5% till 7.5%. For July, September, October and November [-90^0,-70^0] has slightly bigger value in comparison to [70^0, 90^0]. For August and December it is opposite.

Figure 5.3 summarizes the results of Figure 5.1 and Figure 5.2 via 2D histogram. The waves with horizontal wavelength between 4-6 km and a direction of propagation from -30^0 till 30^0 are characterized through the highest percentage of presence during the whole period. It varies from month to month and reaches the highest values in August and the lowest ones in December. The waves with horizontal wavelength from 12 till 14 km show a distribution which looks like a chess table. Waves with horizontal wavelength large than 6 km and a propagation direction of -10^0 to 10^0 are not found. From July till October waves of size between 4 and 6 km have a heavy symmetrical distribution around a propagation direction of 0^0. In November it starts to distort more from [0^0, 90^0] to [0^0, -90^0] direction. December shows more uniform distribution among the wave's size and their directions.

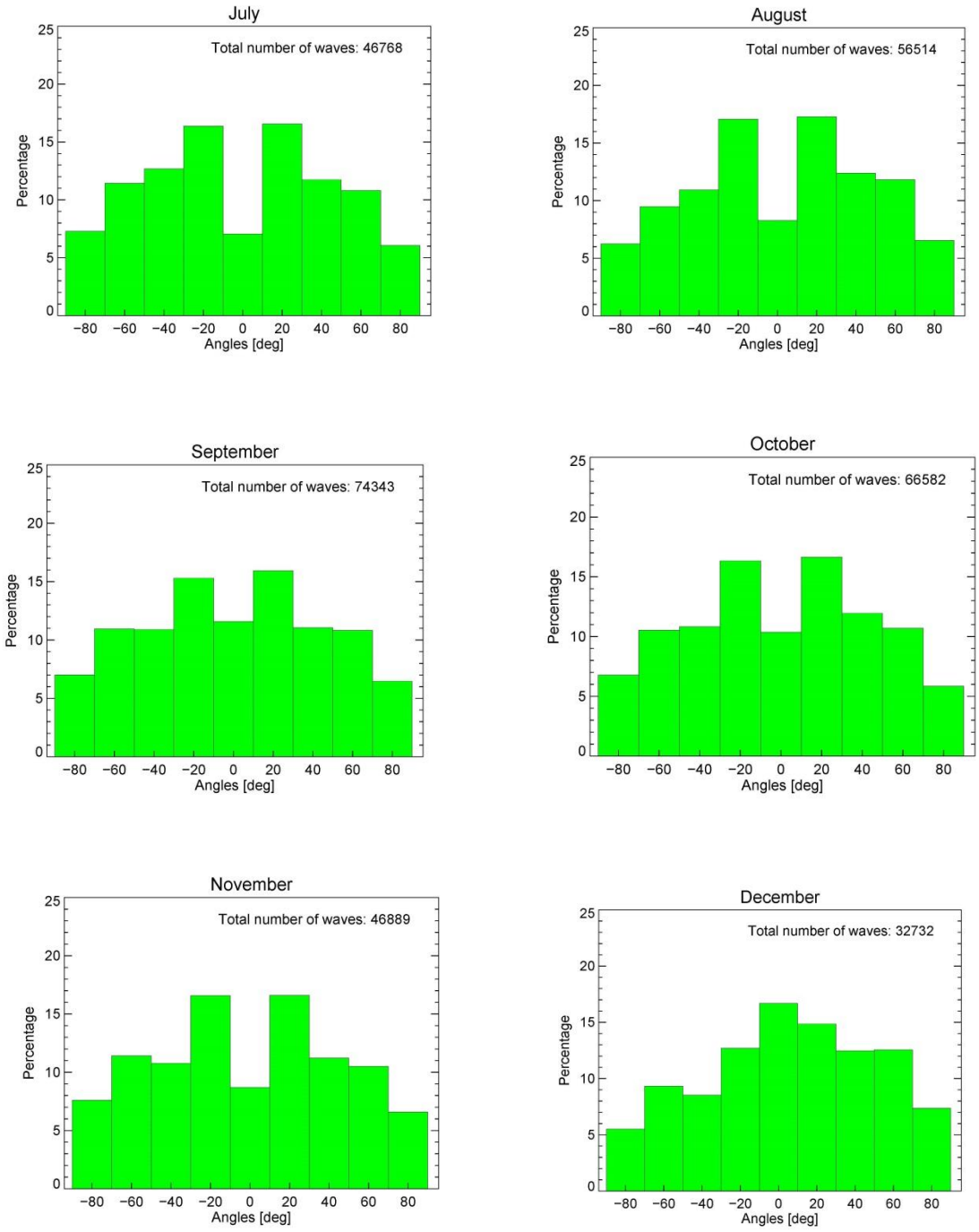

Figure 5.2 Histograms of distribution of the propagation directions for wavelength less than 15 km.

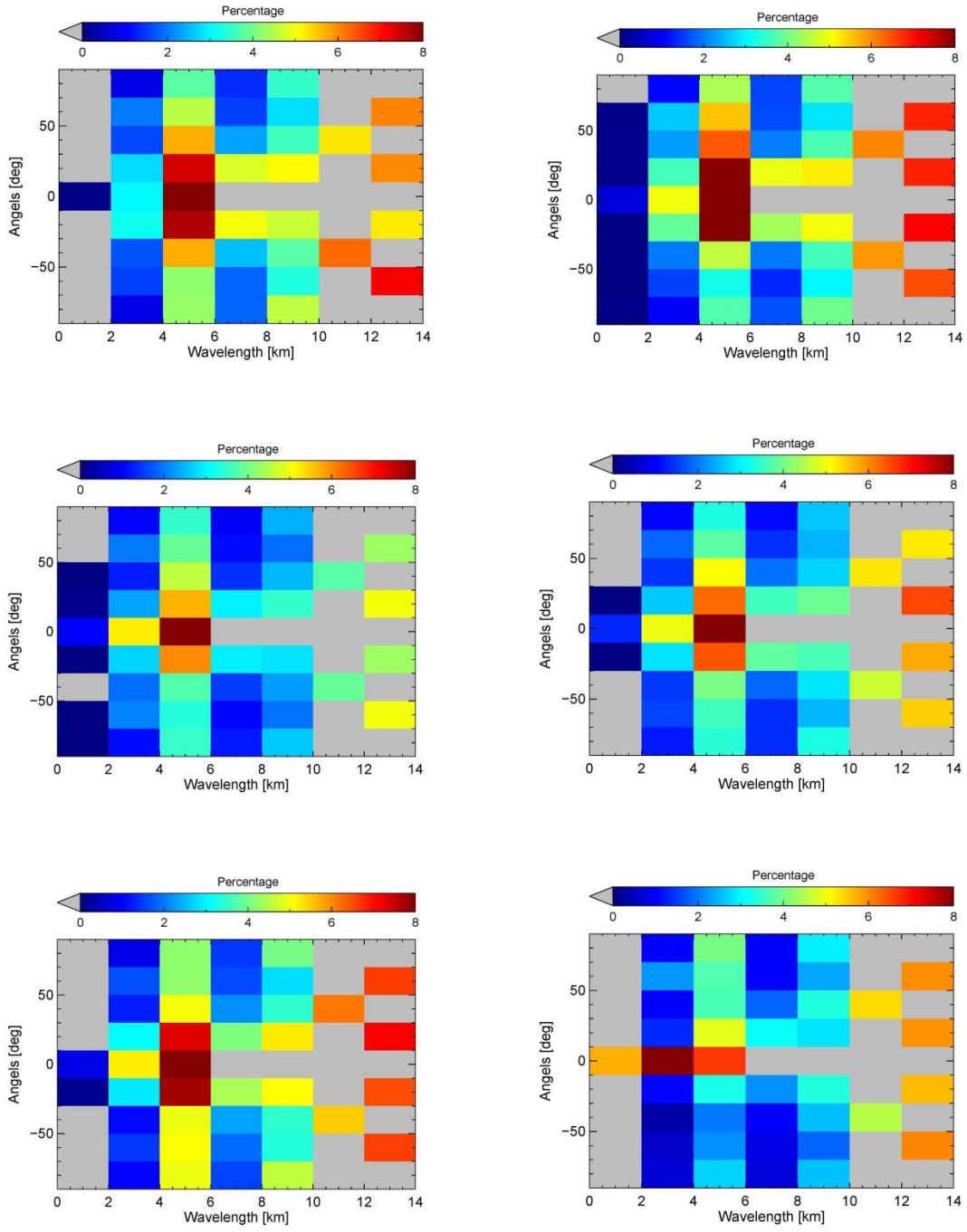

Figure 5.3 2D histogram (horizontal wavelength vs. angle of propagation) for wavelength less than 15 km.

From the direction of propagation and the horizontal wavelength, information about the zonal and meridional wavelength can be calculated Zonal and meridional wavelengths play crucial role for determination the direction of wave propagation across the globe. Zonal wavelength refers to the wavelength along the latitude circle or in the west-east direction. Meridional wavelength describes distribution of wavelength along a meridian or in the north-south direction. The formulas for calculation are following:

$$\lambda_x = \lambda_n \times cos(\alpha) \qquad Eq.\ 5.1$$

$$\lambda_y = \lambda_n \times sin(\alpha) \qquad Eq.\ 5.2$$

where is λ_x zonal wavelength, λ_y is meridional wavelength, λ_n is horizontal wavelength and α is direction of propagation.

Figure 5.4 shows the distribution of meridional wavelengths. Figures show approximately a lognormal distribution. Waves of the range till 2 km in August, September, October and November have a value of 11%. In July it is a little bit less (10%). In December there is a rise till 14%. Waves in a range from 2 till 4 km have the highest percentage of presence. In July it is 35% and continues to rise in August (37%) and reaches its maximum in September (40%), after that it starts to decrease till November (36%). In December there is small jump to 39% again. The waves in the 4-6 km range. In July the value is 25% the same as in November. August, September and October show the same percentage of around 22% +/- 0.5%. Meanwhile, the biggest difference in comparison to previous bin can be seen in December and it equal to 22%. The smallest, which is equal to 10%, is in July. The decrease of values continue for the next bin of 6-8 km wavelength. For the months from July till November the percentage ranges between 12% and 14%. Different to Figure 5.1 waves between 8- 10 km have relatively small percentage amount in the histograms in Figure 5.4. The highest value is during December and equal to 6.5%. During the other months it varies around 6%. Then a small rise can be noticed for the 10-12 km waves. In July it starts from 9% and keep going down till 7%, in October it starts to increase again till 9% in December. After a slight rise goes drop again. For all the months percentage is approximately constant and equal 4% except July where it is 3%.

Zonal wavelength distribution is shown in Figure 5.5. Here figures also show lognormal distribution. In comparison to the meridional zonal wavelength do not have such a big difference between two first bins. Smallest waves have a range of 24-27 % during the given time. Less of them are observed during July and November. In September can be seen value of 27%. As was mentioned before the jump till the next bin is not that big and equal approximately 5%. Horizontal wavelengths with a range between 2- 4 km have stable presentence during the whole time of observations, which is around 29%. The bin with 4-6 km size shows significant fall down around 10% or even more. July and August have 19% value, other months have 17%. Decrease is continuing like it was with meridional wavelength till the bin of the size 10-12 km, then small rise within the bin. In July and September the value is 7%. August and November show 8% result. In November it is 9%

and in December it is 10%. And the last bin gives constant result around the months of 4%. In December it is a slightly bigger (5%).

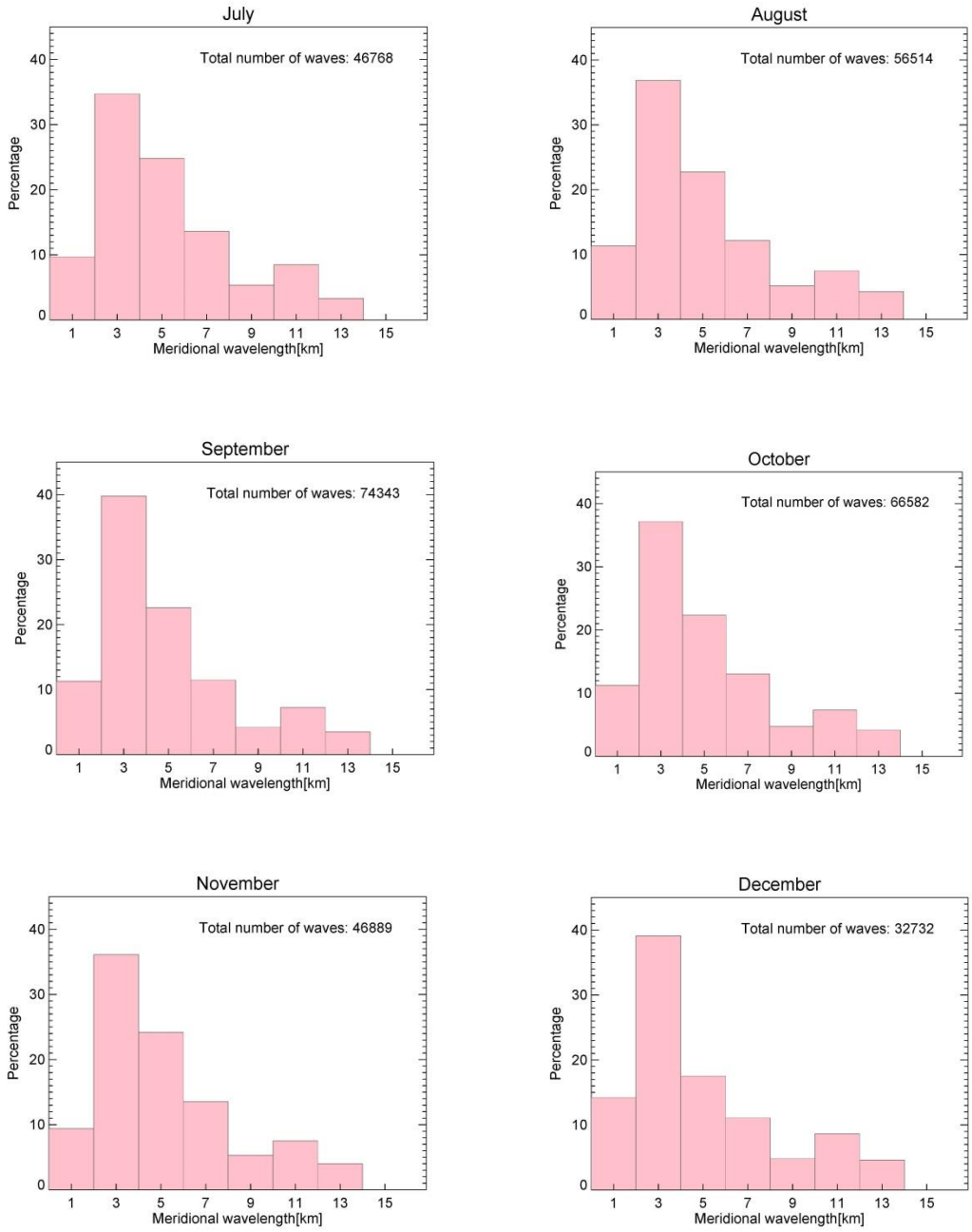

Figure 5.4 Distribution of waves along a meridian for the wavelength less than 15 km.

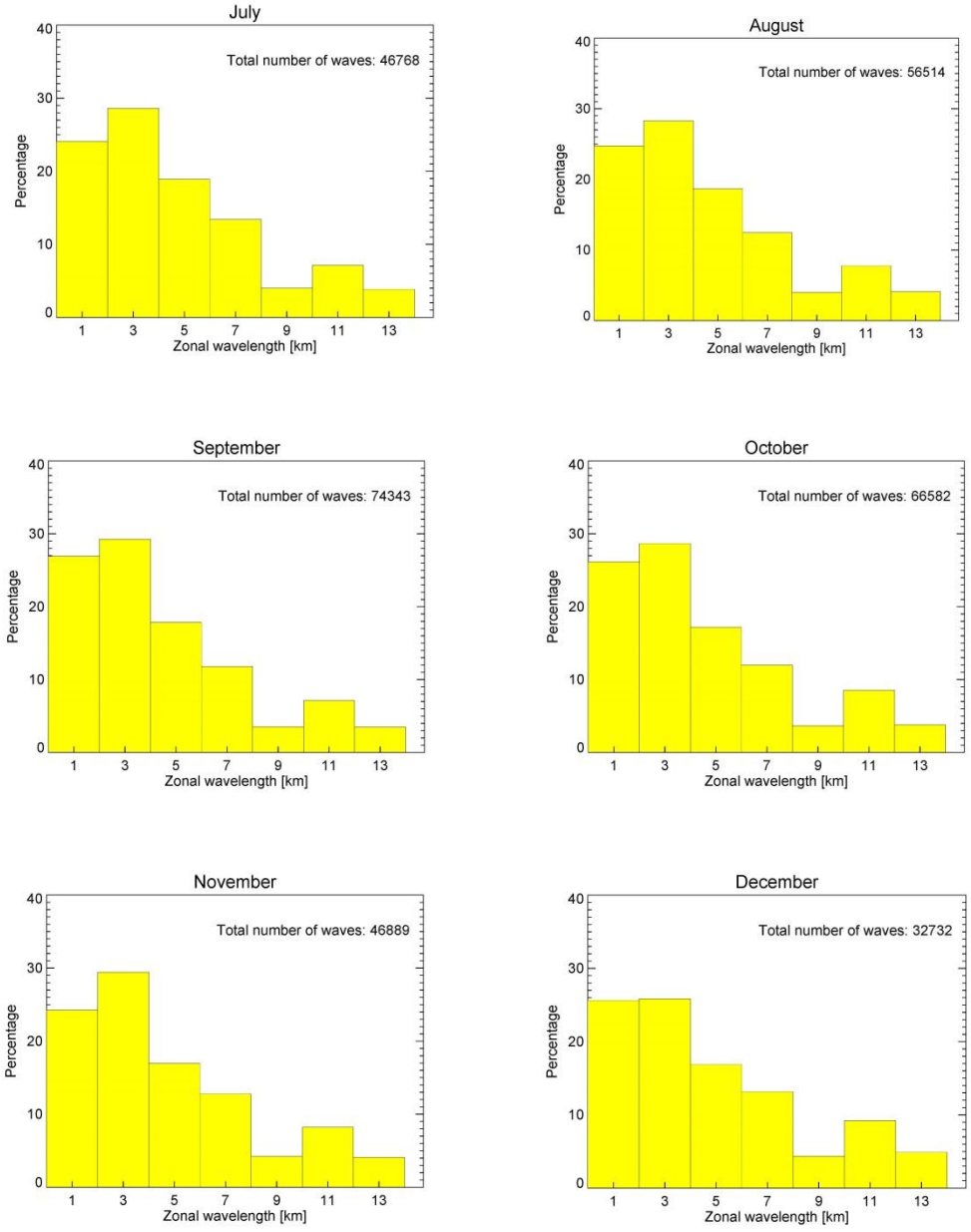

Figure 5.5 Distribution of waves along a latitude circle for the wavelength less than 15 km.

Figure 5.6 shows a 2D histogram (meridional wavelength vs. zonal wavelength). The most concentration of waves is for the smaller waves till 6 km both for meridional and zonal directions. The highest value is in the bin for 2-4 km waves during the whole of the time of observation. The rest is almost always less than 5% of the total amount of data.

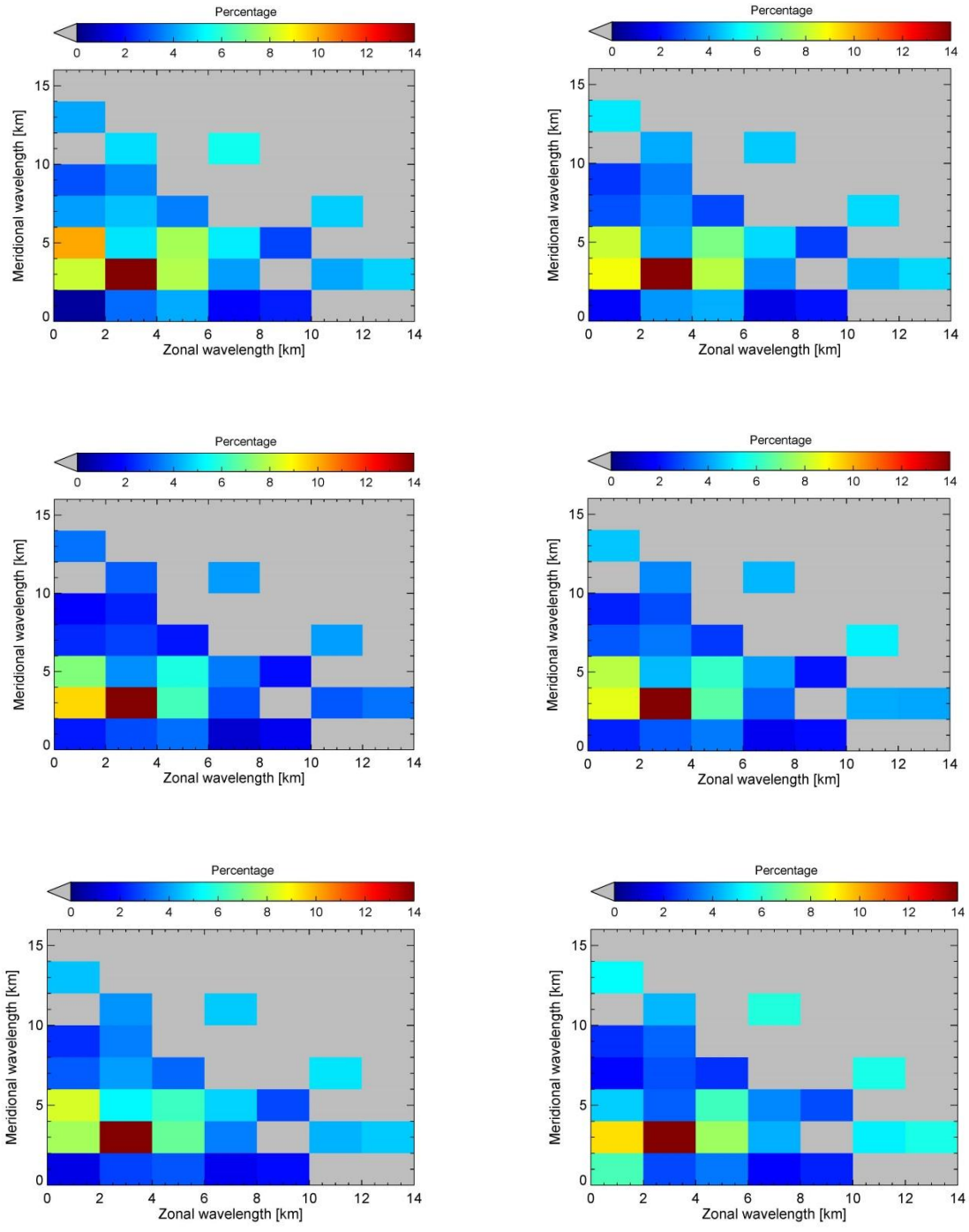

Figure 5.6 2D histogram of the wave distribution in the north-south vs. west-east directions.

5.2. Waves with wavelength in a range from 2 km to 6 km

The analysis showed that waves with horizontal wavelengths from 2 till 6 km are observed most frequently. To have a better overview of these waves Figure 5.7 and Figure 5.8 address this wavelengths in detail. From Figure 5.7 it can be seen that the most of the waves are in the range between 4 and 5 km; their frequency of occurrence percentage is always slightly higher than 40%. November shows the highest amount of wave with the percentage of 44%. Second the most common horizontal wavelength are waves with size from 5 till 6 km. Their values varies from 27% in December till 32% in July. Waves from 3 till 4 km have constant rate of appearance with month, which value is around 20%. The smallest amount belongs to the waves with size 2-3 km. July and November have 5%, August and October are 8%, September is 9%, December has 14%.

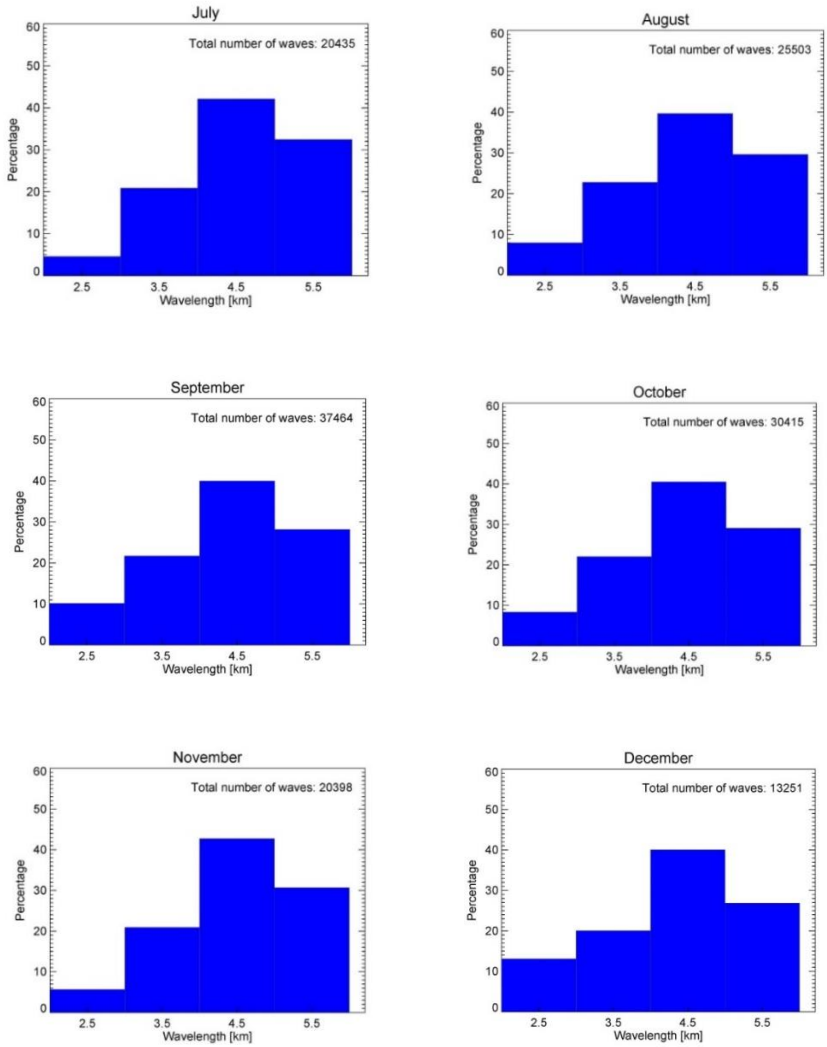

Figure 5.7Histograms of the occurrence of gravity waves events during the observatoin period from July till December with range of wavelength between 2 and 6 km

The angles' distribution for smaller waves is similar to a normal distribution for all months, except December. From July to October the values decrease gradually from 0 degree direction propagation to 90^0/-90^0. In September and October bin with [-10^0, 10^0] direction of propagation has significant higher percentage, 22% and 21% respectively. In November the directions of propagation in [-90^0, -50^0] and [50^0, 90^0] range show nearly constant values between 7%-10%. The main direction of [-10^0, 10^0] degree has 19%. The most unusual distribution can be observed in December. [-10^0, 10^0] degree direction still has the highest value of almost 30% and all their rest values are not higher than 14%.

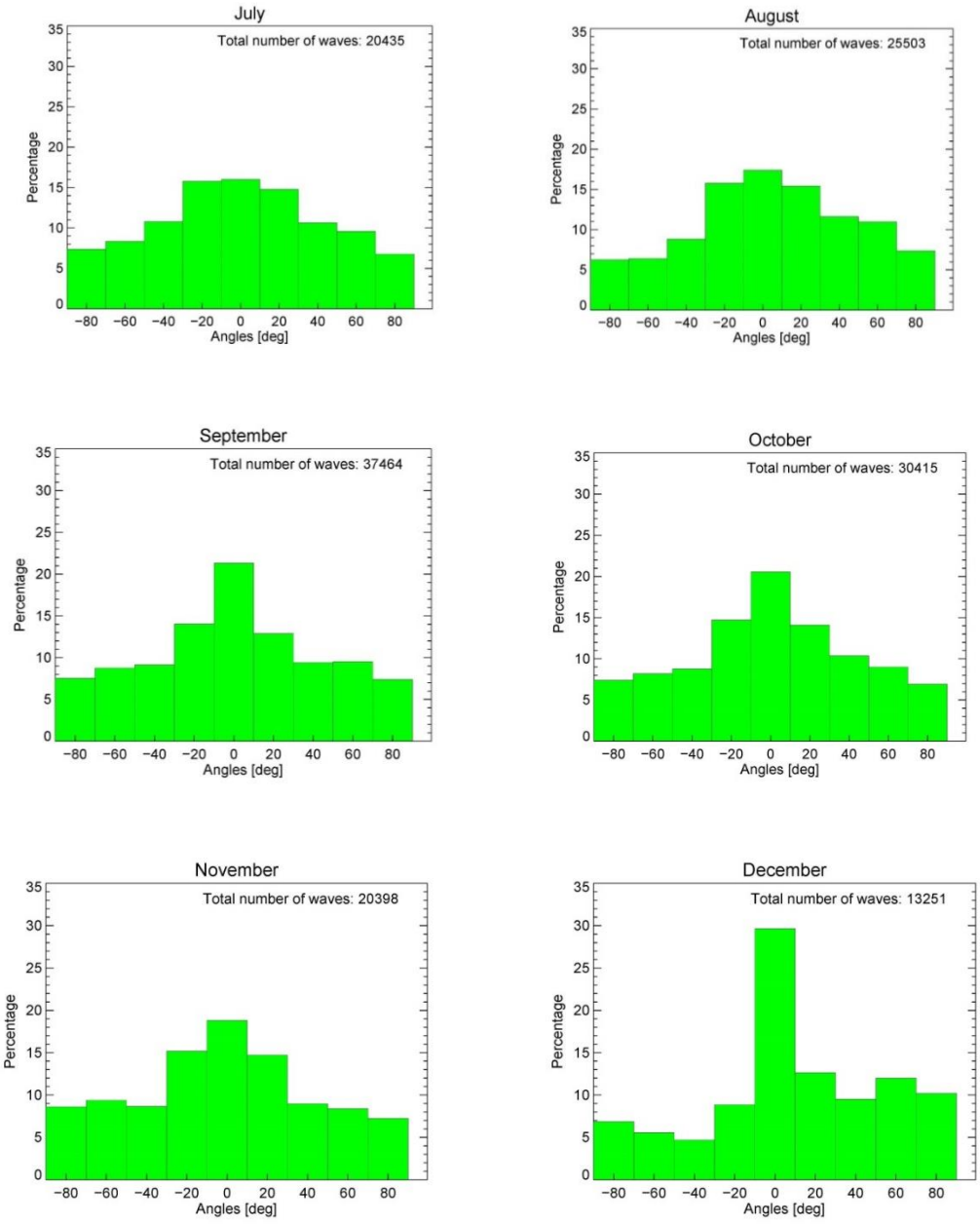

Figure 5.8 Histograms of distribution of the propagation directions for wavelength in the range between 2 and 6 km

5.3. Waves with wavelength smaller than 26 km

The largest horizontal wavelengths that can be extracted from the given images with the FFT algorithm is around 30 km. For that purpose the algorithm was applied to the whole image at once. The wave distribution in this case has a more divers character in comparison to the previous subchapters. As a result the total amount of waves in this case is 73 555. The highest amount is extracted during October and it is 15 213. The smallest amount is 7288 in December.

First thing that catches the eye is the absence of any data for the waves in a range of 16-18 km and 22-24 km wavelength. This happens for the whole data set. Beside that the lowest frequency of occurrence show amount of presentence belongs to waves of the size 2-4 km, which for the whole data set reach barely 1%. 4-6 km waves have stable presentence between 5% and 7%. 7% can be observed during September. Unusual low with 3% is the value for December. Waves of size 6-8 km have a good proportion of appearance during the second half of 2014. July is characterized through the highest value of 16%, than the values decrease slightly (August (14%), September (15%), October (13%)). November shows 14% and December has 11%. The highest values present for the 8-10 km range. It starts from 20% in July, than constantly decreases till 16% in October. November and December have stable value of 18%. For 10-12 km waves the maximum is in July and equals 11%. That means the maximum is for wavelengths between 10 km and 12 km 10% less than the maximum for wavelengths between 8 km and 10 km. Minimum is 8%, which is reached during October and December. For 12-14 km waves there is one more slight reduction for about 1-2%. July, August and November have 8%, September and December have 7% and October has 9%. Waves of size 14-16 decrease a gain for average 4% from values for 12-14 km waves. 18-20 km waves augment their values: July has 14%, August, September and November have 15%, October has 16% and the highest in December 17%. These waves have values that are comparable to the 6-8 km waves. The percentage scales down again for the waves of 20-22 km size. July shows the lowest amount which is 4% and December has the highest (11%). The last bin has waves of size 24-26 km. July and August give 11%. September and October show 12 % amount. November has the less amount of this waves in comparison to the others months, which is 10%, and December has 14%.

Like in Figure 5.2 at Figure 5.10 it can be seen that the direction of propagation in the range $[-10^0, 10^0]$ represents the minimum of this distribution. July and August have highest amount, 5% and 5.5% respectively. The rest of the months show values slightly below 4%. The distribution is approximately symmetric around $[-10^0, 10^0]$. The lowest values are reached for [-90, -70] and [70, 90] degree directions with around 5%. The highest proportion of waves is concentrated in $[-70^0, -10^0]$ and $[10^0, 70^0]$ directions of propagation. Bins of the range $[-50^0, -30^0]$ and $[30^0, 50^0]$ are smaller in comparison to their neighboring bins. Values of bin [-50, -30] degree from July to December reach the following values [13%, 12%, 10.5%, 12%, 11.5%, 9%]. For the bin [30, 50] degree the values are [11%, 13%, 13%, 14%, 11.5%, 14%]. In October both bins have the same value. During the measuring time bin of the range [30, 50] degree has slightly bigger values in comparison to the [-50, -30] degree direction.

Bins with a range [-70^0, -50^0], [-30^0, -10^0], [10^0, 30^0] and [50^0, 70^0] are correlated to each other. Percentage of presentence in this directions are the biggest among the whole data set. Values varies between 14% and 17%. The smallest can be seen for bin [10, 30] degree range in July with value of 13% and the largest is in December with a value of 19% with direction of propagation [50^0, 70^0].

Figure 5.11 is given for visualization and better understanding. It can be seen that waves till 16 km wavelength have more or less proportional distribution. Waves with wavelength from 2 till 5 km in some cases are not present at all or have very small percentage of appearance. Similar to Figure 5.3 there is an absence of any waves in direction of [-10, 10] degrees. For Figure 5.11 this happens for waves with horizontal wavelength of 10 km. The other interesting remark is that the biggest proportion is related to the waves between 18 till 26 km. This waves show the same “picture” of distribution with slightly different percentage from month to month.

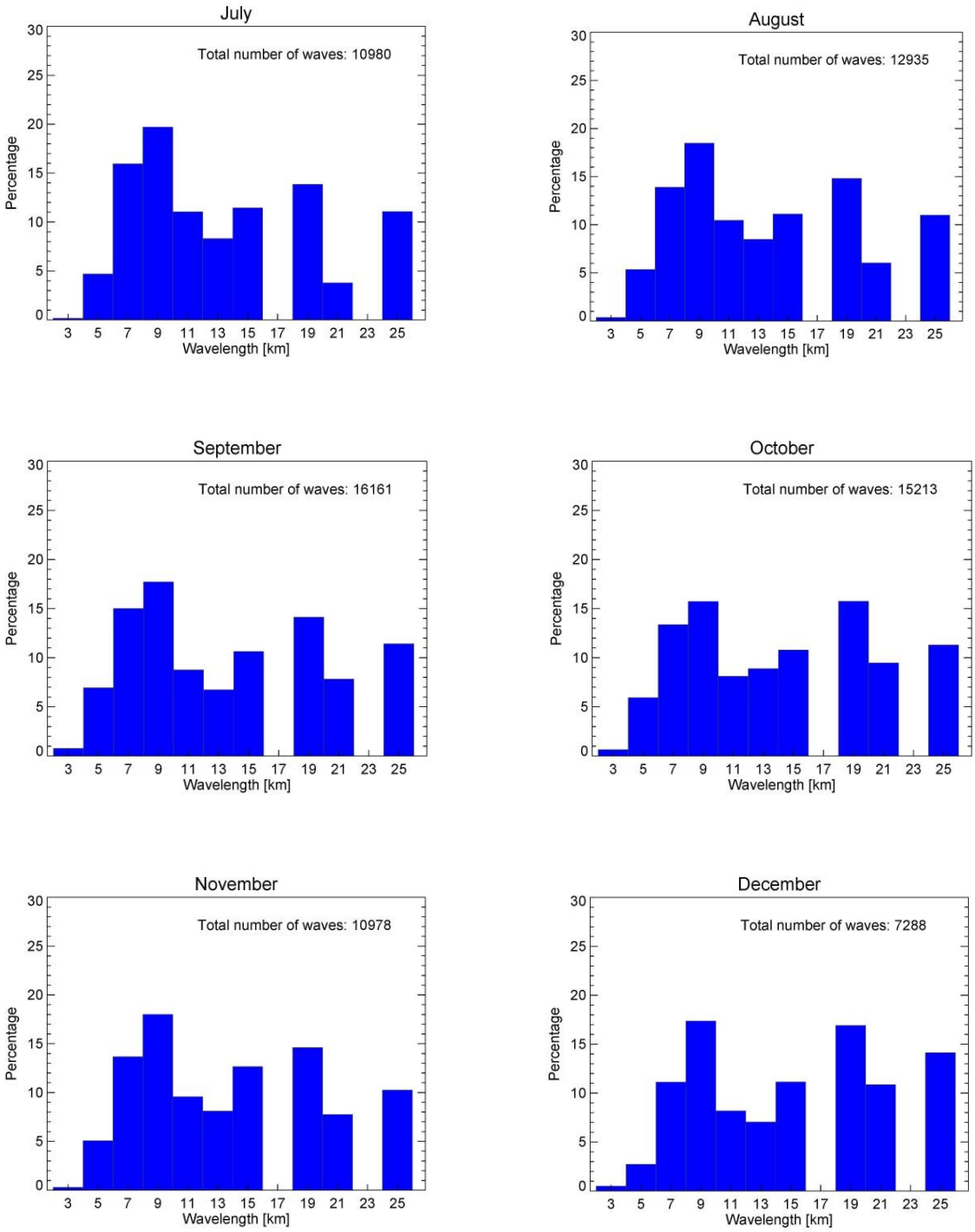

Figure 5.9 Histograms of the occurrence of gravity waves events during the observation period from July till December with range of wavelength till 30 km.

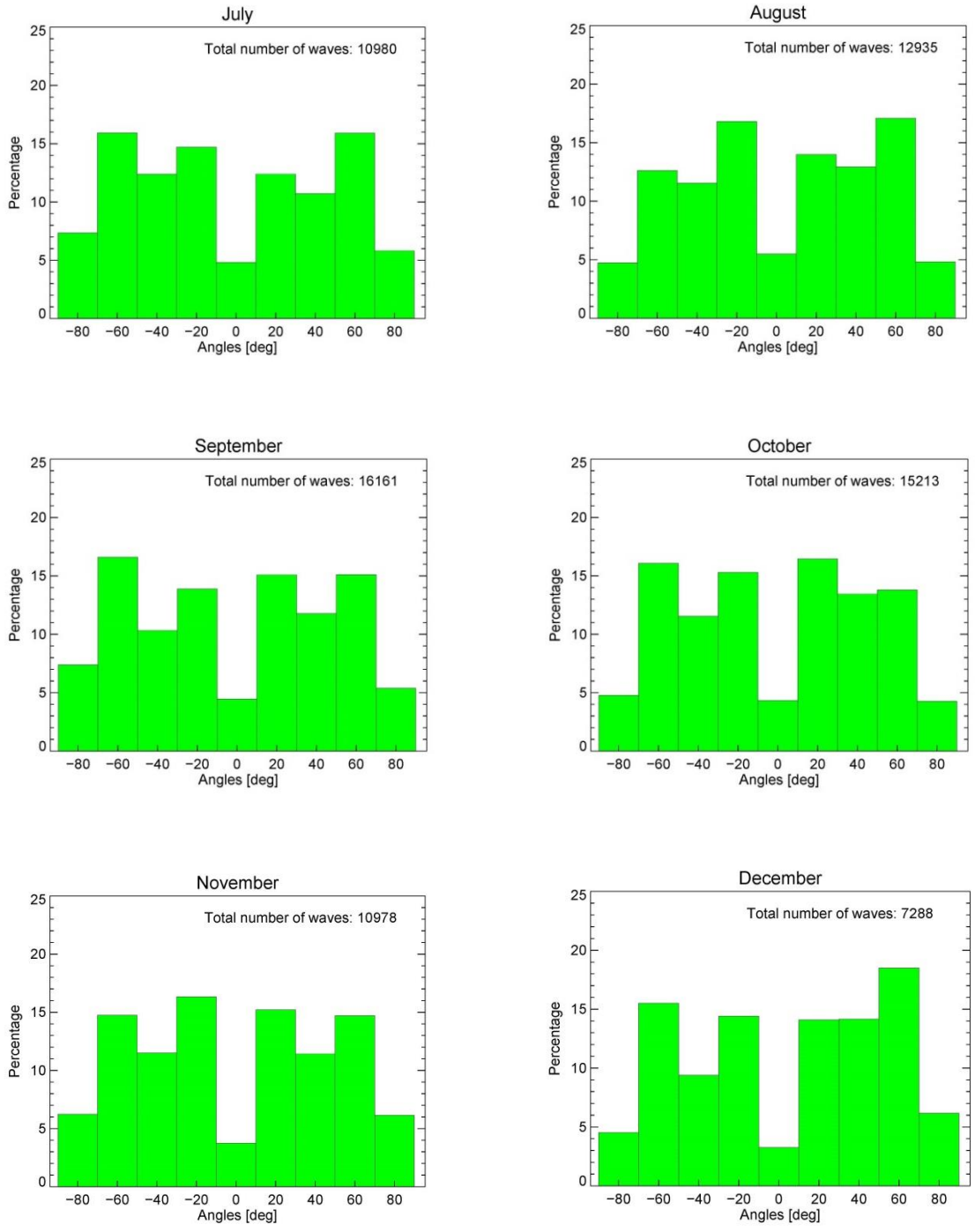

Figure 5.10 Histograms of distribution of the propagation directions for wavelength till 30km.

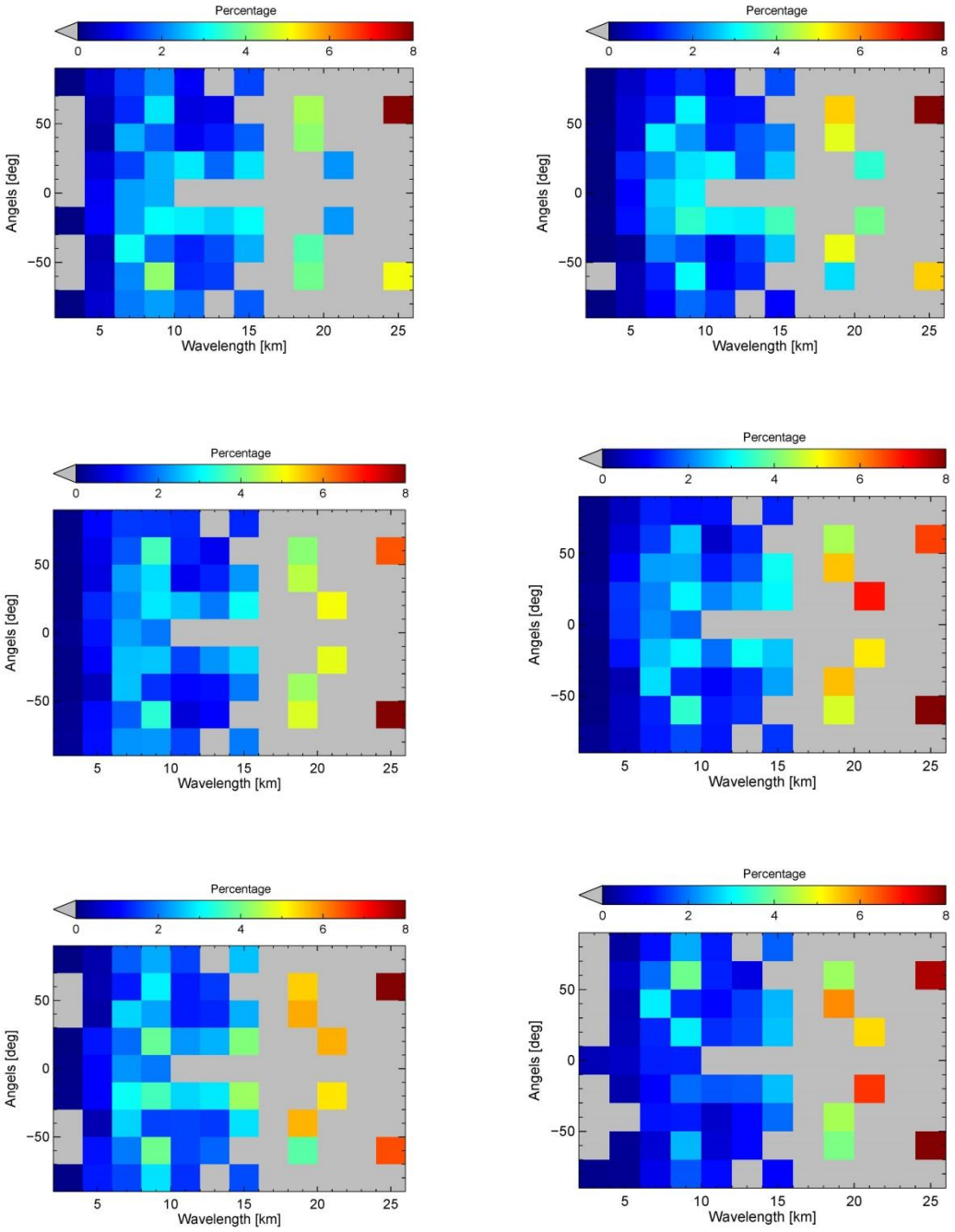

Figure 5.11 2D histogram (horizontal wavelength vs. angle of propagation) for wavelength less than 30 km.

Figure 5.12 shows distribution of the meridional wavelengths. Figures also have a lognormal distribution curve shape like it was with Figure 5.4. Bin size is chosen 2 km as well. Waves of the range 0-2 km and 2-4 km wavelength are really close to each other, The biggest difference is in October and equal to 2.5 %. In July, August, September and December values occur around 15% or a bit higher. In October and November value for the bin of 0-2 km range decreases till 13% and for bin 2-4 km range stays around 15%. The percentage of presentence of waves in a range 4-6 km slightly less in comparison to the neighboring bins and varies between 11-12% for all months except December where the value is falling down till 8%. From 6 till 12 km the values of percentage fall gradually. The bin of size 6-8 km wavelength starts from approximately 15% and falls till the bin of 10-12 km with value around 5%. For July this fall continues till the bin of size 20-22 km with value of 2%. For other months can be seen a small jump in the bin of 12-14 km size. In August this value equal 8%, in September it is 8.5%, in October it is 10%, November and December show us result of 9%. After this slight jump in August, October and November values continue to decrease till the bin of 20-22 km wavelength size. In September and December from this bin starts increasing again. The last bin of 22-24 km wavelength is slightly higher in comparison to previous one for all months. In July, August and November the value is 4.5%. In September and October it reaches 6% and the highest value can be seen in December and it equals 7%. The remarkable thing that can be seen from figures is the absence of and data for the range of 20-22 km.

Zonal wavelength distribution is shown in Figure 5.13. Zonal wavelength figures have lognormal distribution, but in this case curve in not that smooth. Graphs show significant up and down through one bin. Bins have the same size of 2 km. There is also one noticeable thing. It is absence of any values in a range between 20 and 24 km. The first bin of the range between 0-2 km wavelengths has the same value as it is with meridional wavelength and its approximate value is around 15% for each month. For the next bin in comparison to Figure 5.12 is small fall down. The biggest fall of 3.5% belongs to July and October. The smallest value can be seen in December and it is 8%, but the previous value of the bin is 11%. For the bin in a range of 4-6 km can be seen increase of the wave proportion. In the August and September it is 19%; in July, October and November the value is 18% and for December it is 12%. Then can be seen sharp decrease till the bin of 14-16 km range. This drop is equal approximately 15-17% in dependence of each month. The bin of 16-18 km size has growth in value again. The highest jump is in December and it equal 11% and the smallest can be seen in September, where it reaches 8%. The in a range between 18 and 20 km wavelength has values in range from 3% till 5%, with smallest in September and October and the highest in August. The last bin of the value 24-26 km wavelength has slight increase in comparison to the last one. In July and December the values reaches 7%. September and October have 5%. August and November show 6.5% and 6% respectively.

Figure 5.14 shows a 2D histogram (meridional wavelength vs. zonal wavelength). The highest concentration of waves can be seen in the next bins: 24-26 km for zonal wavelength vs. 0-2 km for meridional wavelength and 8-10 km for zonal wavelength vs. 22-24 km for meridional wavelength. The highest concentration can be seen till 15 km wavelength in both directions.

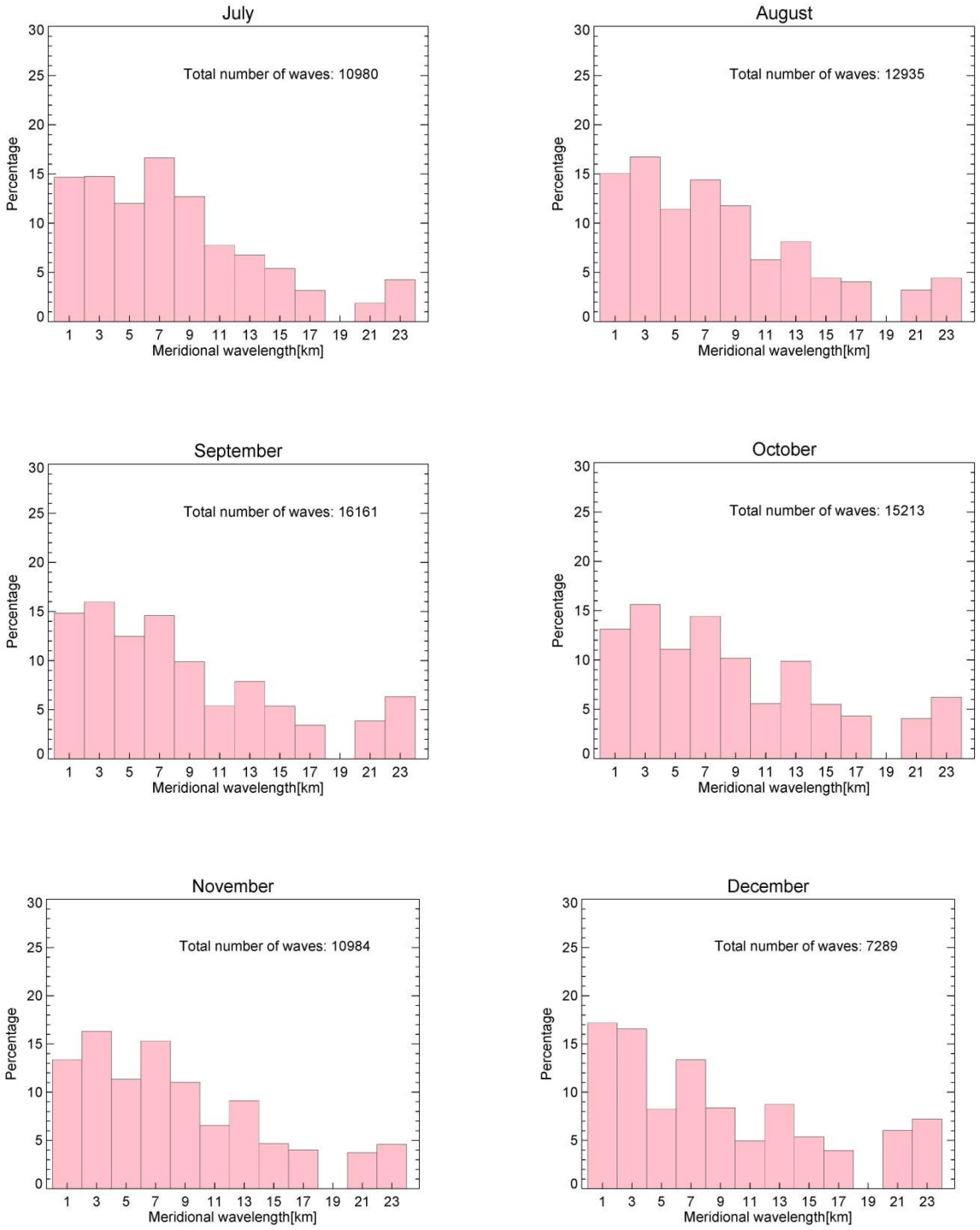

Figure 5.12 Distribution of waves along a meridian for the wavelength less than 30 km.

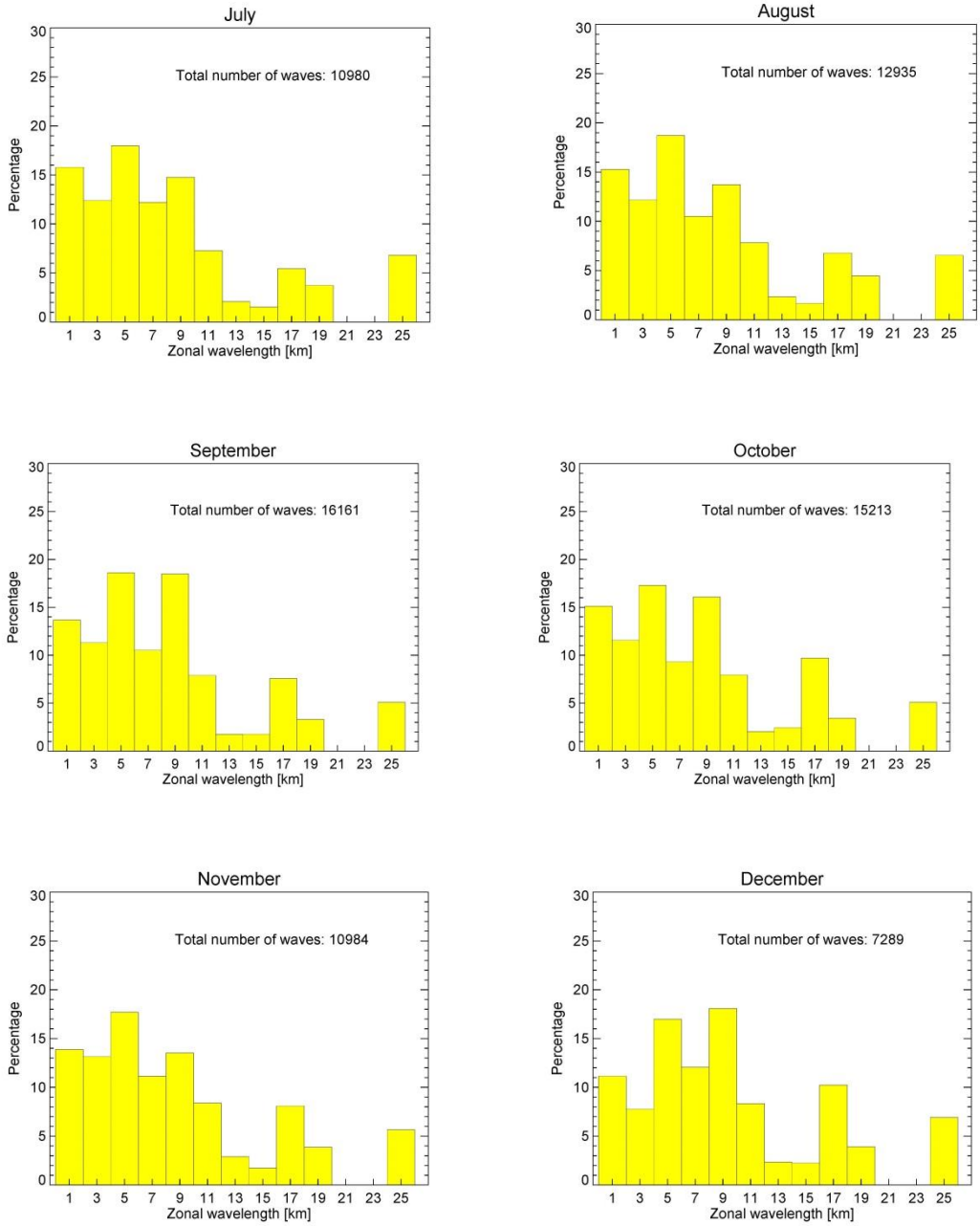

Figure 5.13 Distribution of waves along a latitude circle for the wavelength less than 30 km.

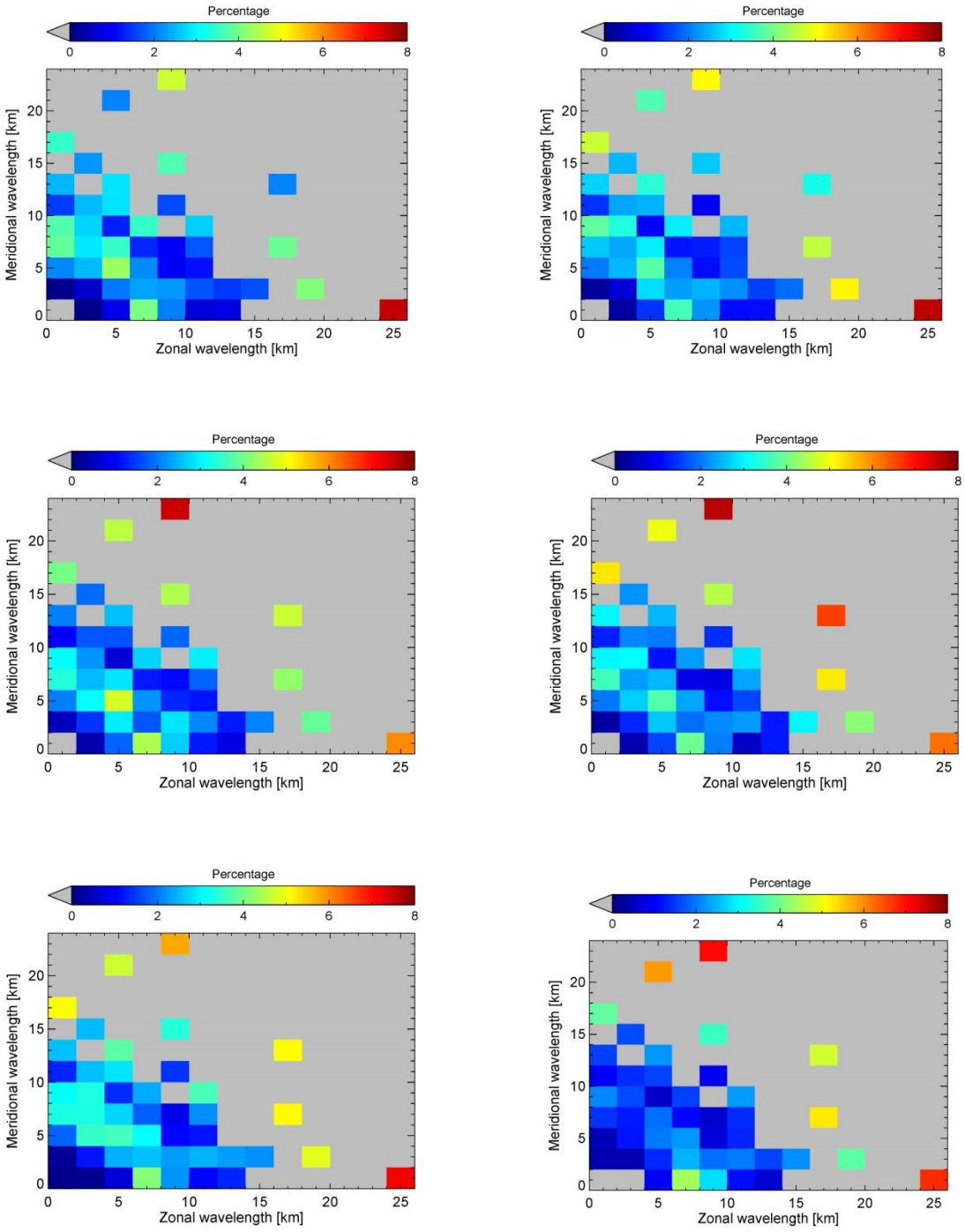

Figure 5.14 2D histogram of the wave distribution in the north-south vs. west-east directions.

6. Discussion

Imaging airglow systems, similar to the one presented in this work, are exceptional suited for measurement and analysis of small-scale gravity waves at the mesopause region, which is difficult to observe with other system. The camera system (used in this work) allows to measure waves till 30 km length. The purpose of this work is to study small-scaled wave structures. There is no clear definition for small-scaled waves. In the literature there are different classifications of the waves according their horizontal wavelength. Taylor et al. (1997) made a classification based on two months of observations in Brazil. According his classification small-scaled waves have 6-18 km horizontal wavelengths. During 18 months of observation in Japan Nakamura et al. (1999) define the upper limit for waves as 17.5 km. Both of this study agreed that the small-scale waves have periods of less 45 minutes. [Peterson, 1979] The period was not investigated during this study, due to a non-equidistant temporal resolution and could be a purpose for future work. The maximum wavelength that is possible to be extracted with the introduced algorithm is 30 km, but in reality the algorithm extracted maximum wavelength of 26 km. In this study waves are classified according to their horizontal wavelengths in the OH images only and considered to be small-scale waves. Because of divers wavelength they are grouped according to 2 km bins.

Small-scaled waves as described above considered to be generated in-situ through shear instability [Taylor and Hapgood, 1990], or through convective instability [Fitts et al., 1993]. Due to the transience of short-lived feature studies of small-scale waves is not frequently published [Taylor et al., 1997]. Other studies have been carried out with simultaneous imager, lidar and radar observations [Hecht et al., 1997] and by numerical modelling by [Fritts et al., 1997]. They found that convective instability induced by a larger scale gravity wave can be the source of such a small-scaled waves. The reason of the appearance of these waves is not investigated in the current work. During the research work of literature have been noticed that unfortunately only short measurements periods were published and there are not that much of studies related particularly to the small-scale waves observations, which gives a motivation for ongoing measurements to improve statistics. For each existing station, where observations for smaller waves have been done, the average of horizontal wavelength for the completed time series and for each season was obtained from different individual publications and combined in the EU-project ARISE. [Keckhut et al., 2014] The results are shown in Figure 6.1.

The time of observation during this study is from July 2014 till the end of December 2014. Because the data does not cover the whole year a seasonal analysis is impossible. Furthermore due to different weather conditions each month contains not equal amount of data. Therefore results are given in percentage for each month. The highest concentration can be observed for waves with wavelength of 2-10 km. The highest amount goes for the waves of 4-6 km size particularly. There are some small difference from month to month at least from August to November but overall the proportion of particular waves is the same. There is also a big proportion of the waves within the range 18-26 km especially for 18-20 km waves. It is a bit less than for the waves 2-10 km but still palpably. Figure 6.1 for the

Europe shows that during spring, autumn and winter mean values of horizontal wavelength are the same and around 3 km. For some mean horizontal wavelength is higher and in between 24-28 km. Nielsen et al. (2009) admitted that there is presently no physical relation, which explains this similarity over different seasons in the observed horizontal wavelengths, periods and phase velocities. It is supposed, that similar-type tropospheric sources, like deep convection, especially at mid- and low-latitudes might be the main sources for short-period waves detected in airglow images.

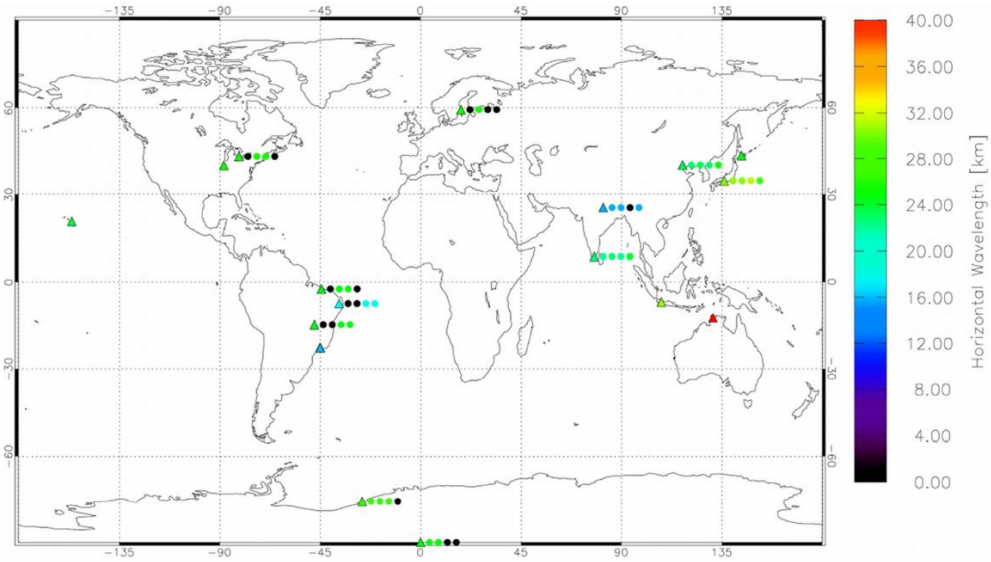

Figure 6.1 Horizontal wavelength. The triangle marks the location of the station, the colour states the mean horizontal wavelength. The dots of each station triangle represent the mean horizontal wavelength for each season, in the following order: spring (March/April), summer (May/August), autumn (September/October) and winter (November/February). [Keckhut et al., 2014]

As was already mentioned in the previous chapter, results of direction of propagation are given in image coordinate system, to receive geographical coordinates 33^0 need to be subtracted from the provided angles. For example, the North direction has 57^0 in image coordinate system. As also already motioned, a direction of propagation is only provided with an ambiguity of 180^0 in this study. To receive exact direction of wave propagation the same wave should be analyzed in a sequent set of images. This option is not provided by the algorithm for now. Due to clouds or fog or lunar influence the temporal resolution of the image series is not equidistant. This complicates the analysis tremendously and could be the scope of further work.

The results for the wave's propagation direction are addressed next. The main directions are NE-SW and E-W for the waves which are analyzed through the windowed FFT. Only in December the main direction is ENE-WSW. However the month December differs from the other ones also cowering the data base. First of all this month contain the less images, because it was one of the most cloudy ones. Secondly, even after removing cloudy nights there are still some nights show events similar to fog. It is also made a statistic

for the waves of 2-6 km size. The results for these waves are different. The main direction is ENE-WSW and data has symmetric distribution in both directions form the main. December shows the highest proportion in the ENE-WSW direction which is ca. 17% higher than the rest of the results. The results, which are based on a non-windowed FFT, give a bit different directions of propagation. To previous directions N-S and ESE-WNW directions are added. The reason might be that waves with wavelength large than15 km are propagate in this directions mainly. According to [Keckhut et al., 2014] the wave propagation exhibits clear seasonal and latitude dependence. The results that were collected from different publications can be seen in Table 3. The propagation angle in the Table 3 is structured in 8 sectors (N, NW, W, SW, S, SE, E, NE) and the preferred direction for each season is given. The data is not complete due to high latitude measurement conditions, unclear or missing information.

Table 3 Seasonal behaviour of gravity wave propagation direction. Only the dominant directions are given. Seasons are defined as follows: spring (March/April), summer (May/August), autumn (Septenber/October), winter (November/February). [Keckhut et al., 2014]

Station	Propagation direction			
	Spring	Summer	Autumn	Winter
Stockholm, Sweden (59.4^{0}N, 18.1^{0}E)	-	N	-	-
Rikubetsu, Japan (43.5^{0}N, 143.8^{0}E)	-	N/NE	-	W
Ontario, Canada (43^{0}N, 81^{0}W)	-	N/E	-	W
Xinglong, China (40.2^{0}N, 117.4^{0}E)	NE	NE	NW/NE	SW
Urbana, IL, USA (40^{0}N, 88^{0}W)	N	N	Evenly distributed	Evenly distributed
Shigaraki, Japan (34.9^{0}N, 136.1^{0}E)	N/E	N/E	Evenly distributed	W
Allahabad, India (25.4^{0}N, 81.8^{0}E)	N/NE	-	-	SW
Maui Hawaii, USA (20.7^{0}N, 156.3^{0}W)	SE/S	NE/E	E/SE	SE/W
Tirunelveli, India (8.71^{0}N, 77.81^{0}E)	N/NE	S/SW	N/NE	N/S
Alcantara, Brazil (2.3^{0}S, 44.5^{0}W)	-	-	NE	-
Tanjungsari, Indonesia(6.9^{0}S, 107.9^{0}E)	S	S	S	E
Cariri, Brazil (7.4^{0}S, 36.5^{0}W)	-	-	NE/S	-
Darwin, Australia (12.4^{0}S, 131.0^{0}E)	SE	N/S	S/SE	S
near Brasilia, Brazil (14.8^{0}S, 47.6^{0}W)	-	-	E	-
Cachoeira Paulista, Brazil (23^{0}S, 45^{0}W)	Evenly distributed	NW	SE	Evenly distributed
Halley Station Antarctica (76^{0}S, 27^{0}W)	NW	S	E	-
South Ploe Station, Antactica (90^{0}S)	-	NE/SW	-	-

According to these research papers the wave propagation directions exhibit not for every station a seasonal dependence. However, it is possible to say that the wave propagation in the northern hemisphere shows mostly a preference for North/ Northeast directions during spring and summer and a western component during winter. During

autumn there are different preferred propagation directions. Approximately the same picture, in some sense, can be seen from presented results. The results give mainly NE-SW and E-W directions of propagation for the waves till 15 km length. For bigger waves till 30 km N-S and ENE-WSW directions are added.

Nielsen et al. (2009) suggested that results might be explained by the process of critical layer filtering of tropospheric gravity waves by the background wind field as they propagate up through the intervening atmosphere into the upper mesosphere. Filtering occurs when the background wind field in the direction of wave motion matches the observed phase speed. He also wrote that a reason for the observed wave directions is strong cyclonic activity over the Weddell Sea. Stockwell and Lowe (2001) found that the dominant direction of the wave propagation may be due to critical layer filtering caused by the seasonally changing background wind field. There is some other suggestion for the reason of the small-scale waves appearance. In the study of Nakamura et al. (2003) over Indonesia state that the reason is the close proximity of strong convective sources that occur immediately to the north of Indonesia for most of the year. For different stations around the world explanation about appearance of the small-scaled gravity waves is different. There are plenty of the natural phenomenon which may be a cause of such behavior and size of gravity waves.

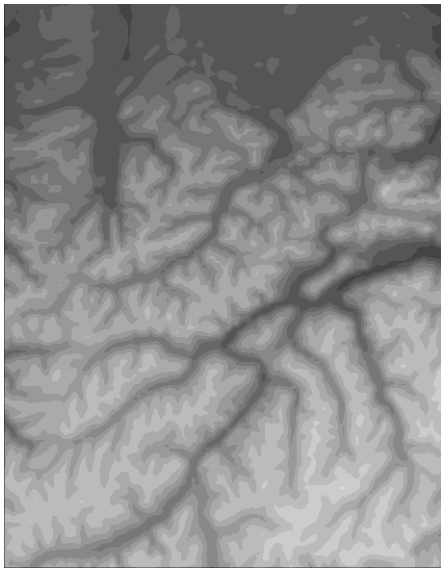

Figure 6.2 The mountains terrain under the region of interest.
[http://topex.ucsd.edu/WWW_html/srtm30_plus.html]

In order to check whether gravity waves reproduce with their horizontal wavelength the mountainous terrain structure. The terrain image under the study area in the atmosphere (see Figure 6.2) is analyzed. The comparison of the results shows that there is no direct connection between the terrain structure and the horizontal wavelength of the analyzed gravity waves, but the reason might be the remoteness of the arear of influence on the shape. The wider area of mountain should be analyzed in order to make a final findings.

Finally it should be noted that aberration and fixed-pattern noise, as mentioned in the previous chapter need to be removed more carefully. Flat-field correction for fixed-pattern noise needs to be adjusted through a better calibration. Aberration can have different values and vary from image to image, so it is very difficult to remove this effects from the results and algorithm still may consider this noise as a wave. Figure 4.14 is taken as a “template” for possible noise, its analysis with FFT reveals the wavelength which are due to this noise and which need to be deleted from the results, but it is still not 100 percent reliable. This procedure as it is carried out in this work may lead also to a deletion of results which are not caused by noise but which show by accident the same wavelength. Partly it might be seen in Figure 5.10 for $[-10^0, 10^0]$ bin size. During the filtering a greater proportion of the data with 0 degree direction of propagation is attributed to noise and removed from statistics. To get more accurate results the preprocessing part should be improved.

7. Conclusion

The basis for this work is an algorithm for two-dimensional analysis of gravity wave structures in all-sky images of the OH-airglow emission. The main purpose of this work is the adaptation of this algorithm for the analysis of OH-airglow images, which are characterized through a relatively narrow field of view but a comparatively high temporal and spatial resolution. This work focuses on the extraction of small-scaled wave structures. The algorithm can be used in two ways. First waves with a maximum wavelength of 15 km are analyzed. Secondly waves with a maximum wavelength of 30 km are in the focus. The algorithm works properly and allows to proceed the whole amount of the data in quite short time period.

OH airglow imager observations are carried out at DLR Oberpfaffenhofen, Germany (48^0 N, 11^0 E) starting January 2014. In this work only the time period from July to December 2014 considered for the analysis. The spatial scales of the waves range from 2 km to 26 km. Wave parameters such as direction of propagation, horizontal wavelength, zonal and meridional wavelengths are investigated monthly.

The distributions of horizontal, meridional and zonal wavelength are approximately similar during the whole observation time with slight variations from month to month. However, differences of the distributions for waves with wavelengths smaller than 15 km and waves smaller than 30 km can be observed. The biggest proportion for waves with wavelengths smaller than 15 km is in a range between 4 and 6 km, for waves with wavelength smaller than 30 km it is between 8 and 10 km. The horizontal propagation direction does not show a clear seasonal variation. Waves with wavelength smaller than 15 km show preferable direction in NE-SW and E-W. Waves with wavelength smaller than 30 km have the same preferential direction plus in addition N-S and ESE-WNW. This is in accordance with previous studies [Nielsen et al., 2009] where a clear seasonal dependence of propagation direction for small-scaled waves was not observed either.

Since the field of view of the OH-camera is located above the Alps the influence of the mountainous terrain on the generation of gravity waves is checked. The hypothesis that the structure of the regular Alpine mountain chains leads to the generation of waves with wavelengths according to the mountainous structure cannot be confirmed.

Concerning the OH-airglow images themselves it is worked out how important a permanent calibration of the data is because effects which are sometimes even not visible by eye can lead to false signals in the data analysis. Since the instrument or an instrument like this is currently planned for a satellite mission, and a 2D-FFT is a standard data analysis procedure, this additional results is of major importance.

References

Alexander M.J., Geller M., McLandress C., Polavarapu S., Preusse P., Sassi F., Sato K., Eckermann S., Ern M., Hertzog A., Kawatani Y., Pulido M., Shaw T.A., Sigmond M., Vincent R., Watanabe S. (2010) Recent developments in gravity waves effects in climate models and the global distribution of gravity waves momentum flux from observations and models. Quarterly journal of the royal meteorological society, 136, 1103-1124

Andrews D.G. (2005) An introduction to atmospheric physics. Cambridge University Press.

Bates D.R. and Nicolet M. (1950) Atmospheric hydrogen. Astronomical Society of the Pacific, 106-110

Craparo R.M. (2007) Significance level. In Salkind, Neil J. Encyclopedia of measurement ans statistics 3. Thousand Oaks, CA: SAGE Publications, 889-891

Fritts D.C., Isler J.R., Thomas G., Andreassen O. (1993) Wave breaking signatures in noctilucent clouds. Geophysical Research Letters, 20, 2039-2042

Fritts D.C., Isler J.R., Hecht J.H., Walterscheid R.L., Andreassen O. (1997) Wave breaking signature in sodium densities and OH nightglow, 2. Simulation of wave and instability structure. Journal of Geophysical research, 102, 6669-6684

Fritts D.C. and Alexander M.J. (2003) Gravity wave dynamics and effects in the middle atmosphere. Review of Geophysics, 41

Garcia F.J., Taylor M.J., Kelley M.C. (1997) Two-dimensional spectral analysis of mesospheric airglow image data. Applied Optics, 36, 7374-7385

Hannawald P. (2014) Aufbau eines Infrarotkamerasystems zur Messung von atmosphärischen Schwerewellen und Infraschall im OH-Nachtleuchten. Master thesis. University of Augsburg, Departament of Physics

Hartmann W.M. (1997) Signals, sound and sensation. Springer Science and Business Media.

Hecht C.S. and Taylor M.J. (1998) Observational limits for lidar, radar and airglow imager measurments of gravity wave parameters. Journal of Geophysical Research, 103, 6427-6437

Houghton J. (2002) The physics of atmospheres. Cambridge University Press.

Keckhut P., Dalaudier F., Mze N., Khaykin S., Angot G., Wüst S., Schmidt C., Bittner M., Le Pichon A., Blanc E., Rüfenacht R., Kämpfer, Sindelarova T., Lastovicka J., Charlton Perez A. (2014)

Benefits of the 3-technique combination for climate monitoring. Deliverable 3.3, EU-project ARISE (Atmospheric Dynamic Research InfraStructure in Europe), Grant Agreement № 284387

Khomich V.Y., Semenov A.I., Shefov N.N. (2008) Airglow as an indicator of upper atmospheric structure and dynamics. Springer Science & Business Media.

Nakamura T., Higashikawa A., Tsuda T., Matsushita Y. (1999) Seasonal variations of gravity wave structures in OH airglow with a CCD imager at Shigaraki. Earth, planets and space, 51.7-8, 897-906

Nakamura T., Aono T., Tsuda T., Admiranto A.G., Achmad E., Suranto (2003) Mesospheric gravity waves over a tropical convective region observed by OH airglow imaging in Indonesia. Geophysical Research Letters, 30(17), 1882

Nielsen K., Taylor M.J., Hibbins R.E., Jarvis M.J. (2009) Climatology of short-period mesospheric gravity waves over Halley, Antarctica (760S, 270W), Journal of Atmospheric and Solar-Terrestrial Physics, 71, 991-1000

Jacobson R., Ray S., Attridge G.G., Axford N. (2000) *Manual of Photography*. Taylor and Francis.

Pearsall T.P. (1980) $Ga_{0.47}In_{0.53}As$: A Ternary Semiconductor for Photodetector Applications. IEEE Journal of Quantum Electronics, 16, 709-720

Peterson A.W. and Kieffaber L.M. (1973) Infrared photography of OH airglow structures. Nature, 242, 321-322

Peterson A.W. (1979) Airglow events visible to the naked eye. Applied optics, 18, 3390

Press W.H., Teukolsky S.A., Vetterling W.T., Flannery B.P. (2007) Numerical Recipes 3rd Edition: The Art of Scientific Computing. Cambridge University Press.

Roach F.E. and Meinel A.B. (1955) The height of the nightglow by the van Rhijn method. American Astronomical Society, 122, 530-553

Rousselot P., Lidman C., Cuby J.G., Moreels G., Monnet G. (2000) Night-sky spectral atlas of OH emission lines in the Near-Infrared. Astronomy and Astrophysics, 354, 1134-1150

Snively J.B., Pasko V.P., Taylor M.J. (2010) OH and OI airglow layer modulation by ducted short-period gravity waves: Effects of trapping altitude. Journal of Geophysical Research: Space Physics, 115.A11, 1978–2012

Stockwell R.G. and Lowe R.P. (2001) Airglow imaging of gravity waves 2. Critical layer filtering. Journal of Geophysical Research, 106, 17205-17220

Taylor M.J. and Hapgood M.A. (1990) On the origin of ripple-type wave structure in the OH nightglow emission. Planet. Space Science, 38, 1421-1430

Taylor M.J., Pendleton W.R., Clark Jr. S., Takahashi H., Gobbi D., Goldberg R.A. (1997) Image measurments of short period gravity waves at equatorial latitudes. Journal of Geophysical Research, 102, 26283-26299

Xenics (2013) User Manual – Xeva FPA Cameras *ENG-2013-UMN002-R002*. Ambachtenlaan 44, *BE-3001* Leuven, Belgium.

Zhao L., Hu W., Cui L. (2012) Face recognition feature comparison based SVD and FFT. Journal of Signal and Information Processing, 3, 259-262

Websites:

Leibniz Institut für Atmosphärenphysik: www.iap-kborn.de Download:16. October 2015

Exelis Visual Information Solutions: www.exelisvis.com Download:16. October 2015